UNIVERSITÀ DEGLI STUDI DI ROMA

"TOR VERGATA"

FACOLTA' DI FISICA

DOTTORATO DI RICERCA IN

FISICA

XX CICLO DEL CORSO DI DOTTORATO

# Raman Spectroscopy on Nanostructures

Eugen Speiser

Tutor: Prof. Wolfgang Richter

Coordinatore: Prof. Piergiorgio Picozza

# Contents

**List of Publications**

1. M. DE CRESCENZI, F. TOMBOLINI, M. SCARSELLI, S. DEL GOBBO, SPEISER E., P. CASTRUCCI, M. DIOCIAIUTI, S. CASCIARDI, E. GATTO, M. VENANZI. Visible and near ultraviolet photocurrent generation in carbon nanotubes. SURFACE SCIENCE. vol. 601, pp. 2810-2813 (2007)

2. P. PAIANO, P. PRETE, SPEISER E., N. LOVERGINE, W. RICHTER, L. TAPFER, A.M. MANCINI. GaAs nanowires grown by Au-catalyst-assisted MOVPE using tertiarybutylarsine as group-V precursor. JOURNAL OF CRYSTAL GROWTH. vol. 298, pp. 620-624 (2007)

3. P. CASTRUCCI, F. TOMBOLINI, M. SCARSELLI, SPEISER E., S, DEL GOBBO, RICHTER W, M. DE CRESCENZI, M. DIOCIAIUTI, E. GATTO, AND M. VENANZI. Large photocurrent generation in multiwall carbon nanotubes. APPLIED PHYSICS LETTERS. vol. 89, pp. 253107 (2006)

4. SPEISER E., K.FLEISCHER AND W.RICHTER, Epioptics-8, Raman scattering as an epioptic probe for low dimensional structures, Proceedings of the 33rd Course of the International School of Solid State Physics, editor: A. Cricenti, p.92-115, 2006.

5. SPEISER E., B. BUICK, S. DELGOBBO, D. CALESTANI AND W. RICHTER, High spatial resolution Raman scattering for nano-structures, Epioptics-9, Proceedings of the 38th Course of the International School of Solid State Physics, editor: A. Cricenti, accepted.

6. SPEISER E., T. SCHMIDTLING, K. FLEISCHER, N. ESSER, ANDW. RICHTER. In-situ Raman Spectroscopy on III-V semiconductors at high temperature in MOVPE. PHYSICA STATUS SOLIDI C. vol. 8, pp. 2949-2955 (2003)

Contributions to Conferences

1. SPEISER E., B. BUICK, S. DELGOBBO AND W. RICHTER, Raman Spectroscopy with High Spatial Resolution, invited talk, Seminar of Prof.Dr. M. Kneissl Group at the TU Berlin, "Heimbach XXI" 1-5.10.2007.

2. SPEISER E. Raman spectroscopy from quasi 1-dimensional nanostructures, MMD Genova 22-25.06.2005.

3. SPEISER E., T. SCHMIDTLING AND W. RICHTER, Anharmonic decay of optical phonons in III-V semiconductors at temperatures up to 1200 K, "Deutsche Physikalische Gesellschaft" Spring Meeting Berlin, DS 24.3, 04.03.-09.03.2005,

4. SPEISER E., T. SCHMIDTLING, K. FLEISCHER AND W. RICHTER, In-situ Ramanspektroskopie beim GaAs-Wachstum in der MOVPE (In-situ Raman spectroscopy of GaAs growth in the MOVPE ), "Deutsche Physikalische Gesellschaft" Spring Meeting Dresden, HL 40.9, 24-28.03.2003.

5. SPEISER E., T. SCHMIDTLING, K. FLEISCHER AND W. RICHTER, In-situ Hochtemperatur-Ramanspektroskopie an III-V Verbindungen in der MOVPE (In-situ high temperature Raman spectroscopy on III-V compounds on the MOVPE (Metal Organic Vapour Phase Epitaxy)), "Deutsche Physikalische Gesellschaft" Spring Meeting Regensburg, HL 38.39, 11-15.03.2002.

6. SPEISER E., N. BLUETHGEN, K. FLEISCHER D. PAHLKE, B. RAEMER AND W. RICHTER, Raster-Nahfeldmikroskopie (SNOM) der Photolumineszenz von Halbleiterquantendots bei tiefen Temperaturen (Scanning near field microscopy of semiconductor quantum dots photoluminescence at low temperature), "Deutsche Physikalische Gesellschaft" Spring Meeting Regensburg, HL 38.28, 27-31.03.2000.

# Chapter 1

# Introduction

One of the most current and also most promising fields of research in solid state physics is that of nano-structured materials. In particular, there is a great interest in nanostructured semiconductors, thanks to the latest developments in preparation methods like MOVPE (Metal Organic Vapor Phase Epitaxy), MBE (molecular beam epitaxy) [1], lithography and colloidal chemistry [2]. These techniques allow to prepare nano-sized semiconductors with excellent crystalline structure and most often also with epitaxially determined orientations with respect to a template. Due to the reduced size, the wave length of elementary excitations within nano-structures (e.g. excitons, phonons) are in the order of the dimension of the nano-structure (de Broglie -, phonon wave length). In this case quantization becomes an important factor, modifying material properties based on those elementary excitations (electronic and phononic density of states). In fact, the interest in nano-structures is triggered by the discovery that their physical properties (electronic, optical, thermodynamical) are different from those of the corresponding bulk material due to confinement. Consequently, the size becomes a new design parameter. This opens a wide potential outlook to technological applications such as light emitting devices, photovoltaic cells and single electron transistors.

For 2-dimensional nanostructures (thin layers, quantum wells), which

already have been prepared for more than two decades by the standard epitaxial techniques (MBE, MOVPE), most of the standard surface science techniques could be applied. As a consequence there is excellent knowledge about their physical properties and accurate comparison with theory. However, to obtain measurements from 1-dimensional (quantum wires, nanorods, nanotubes) and 0-dimensional nanostructures (quantum dots), the additional requirement occurs that the probe must provide lateral resolution in the nanometer range. This requirement excludes or limits many of the standard surface science techniques and is especially true for the standard optical tools with diffraction limited spatial resolution just in the sub-micrometer range. If possible, the parameters of the growth process of the nanostructures in question are modified in order to reduce the spatial density of the nanostructures in a way that only one structure is contained in the probing area. However, this creates an artificial or at least a different growth process and is not always possible.

On the other hand there is a great need for optical and spectroscopic analysis of nanostructures, as has already been demonstrated for bulk semiconductors, in order to determine the electronic and vibrational properties. Because of confinement effects they will be different from those of the bulk and thus open the possibility to test the fundamental theoretical aspects as well as envision new technological applications.

Of course sufficient spatial resolution is clearly provided by scanning probe microscopes (SPM). The STM (scanning tunnelling microscope) [3] in particular is an extremely valuable tool for study the nano-structures. Already some time ago the SPM technique has been adapted to a SNOM (Scanning Near field Optical Microscope) where the sub-wavelength resolution obtainable using optical glass fiber tips with a small aperture ($< 100nm$) was exploited [4]. Spatial resolution in the nm-range was obtained.

However, for optical spectroscopy this solution has an essential draw-

back. The intensity that is transmitted trough the aperture depends strongly on its size. In practice to obtain sufficient signal levels a reasonably large aperture size ( $100nm$) should be chosen. On the other hand for nanometer range resolution a smaller aperture size is needed. Consequently a compromise is necessary to obtain sufficient resolution at a reasonable signal to noise ratio [5, 6]. Thus, in seeking for improved spatial resolution one has a serious signal to noise ratio problem. For Raman scattering which is our main interest here, as a higher order optical process, this means that only few successful experiments have been performed up to now by small aperture SNOM on strong scattering materials [7, 8].

A few years ago, however, an apertureless version of the SNOM, named a-SNOM, has been presented which does not have these intensity problems [9]. The a-SNOM worked with a sharp silicon tip on a AFM (atomic force microscope [10]) cantilever. In addition, when the tip is made from materials supporting surface plasmons in the spectral range of interest, this can lead to a strong electric field enhancement which can be very much localized, depending on the apex radius (sharpness) of the tip. The A-SNOM technique using this enhancement effects has been applied also quite recently to Raman scattering with either a modified AFM with a metallized cantilever [11, 12] or with a sharp silver tip [13] for enhanced signals from molecules and has been termed in that case Tip Enhanced Raman Scattering (TERS) .

The goal of this work is to study nano-structures by optical methods, especially by Raman spectroscopy. 1-dimensional nano-structures were in the main focus because of their recently intensively investigated and improved growth mechanisms. This research enabled the synthesis of high crystalline quality, controlled orientation and size. Samples from collaborating groups were available for our optical spectroscopy investigations. If possible, the measurements are performed on single nano-structures in order to exclude averaging of their properties by summing contributions from different structures.

This is achieved by using confocal microscopy spectroscopy providing diffraction limited spatial resolution in the micrometer range ( $1\mu m$).

Another important goal of this work was to design and to build a new experimental set-up in order to extend the spatial resolution to the nanometer range, exploiting near field optics in combination with scanning probe microscopy (Scanning Tunnelling Microscopy and Atomic Force Microscopy). This would enable simultaneous measurements of topography and spectroscopy, thus permitting direct correlation of morphological and optical properties. Moreover the internal structure of nano-samples could be accessible by optical spectroscopy.

# Chapter 2

# Nanostructures

Silicon solid state devices mark the beginning of an electronic technological revolution. Most of the early semiconductor devices were fabricated from bulk crystalline material. But as the quest for rugged high performance and high speed devices developed, miniaturization became important and integrated devices built on large wafers emerged using lithography to pattern many devices per unit area. The progress in the last three decades can be characterized by a gradual replacement of Si devices by thin epitaxial film and multilayered structures (two dimensional) with special properties. These structures have led to the development of Field Effect transistors such as High Electron Mobility Transistors (HEMT), quantum well lasers, optical modulators, *nipi*-photosensitive elements, quantum well photo detectors, avalanche photodiodes etc. In these quasi-two dimensional systems, most of the electronic and vibrational properties are different compared to that of the bulk crystal, mainly due to the so-called quantum size effects. The most dramatic changes in properties take place in the structures where the carriers/phonons are confined in the region of a characteristic length of the order of the electron/phonon wave function wave length.

If the motion of a particle (or quasi particle), e.g. electron or phonon, is restricted in one or more dimensions by a potential well, this particle is confined in the well because the probability to traverse the

energy barriers is lower than to remain within it. When the confining dimension is large compared to the wavelength of the particle, the particle behaves within the confined area as if it were free. As the confining dimension decreases and reaches the order of the wave function wave length, the particle's energy states are modified due to the overlap of the wave function amplitude reflected from the barriers. This is defined as "quantum confinement".

The free path length of particles in solids is usually much longer than the particles wave function wave length. In case the confined dimension reaches the order of the free path length no "quantum size" effect takes place. However, other characteristics of the particle like lifetime and mobility are affected changing e.g. the carrier and heat transport properties.

A quantum well (thin layer) is a structure that confines in one dimension, a quantum wire confines in two dimensions and quantum dot (e.g. a small sphere) in all three dimensions.

The past decade has also witnessed a revolution in the science and technology of one-dimensional systems: semiconductor nanowires and carbon nanotubes. These nanoscale, 1-dimensional structures have stimulated great interest due to their importance in basic scientific research and potential technological applications . Many unique and fascinating properties have been proposed and demonstrated for a class of materials such as metal-insulator transition, superior mechanical toughness, high luminescence efficiency, enhancement of thermoelectric figure of merit and a low lasing threshold. These one dimensional structures can also be used as the building blocks to assemble new generations of nanoscale electronic circuits and photonics.

## 2.1 Electronic and optical properties of nano structures

Electronic and phonon confinement have been the subject of extensive studies in the past decade. The electronic quantum size effect is mostly detected as a shift of the interband absorption or luminescence peak to higher energies [14]. This is normally observed in quantum wells, quantum wires or in quantum dots.

Low dimensional systems with one (quantum wells) and two dimensional (nano wires) confinement have a mixed discrete-continuum energy spectrum associated with a 1- and 2- directional confinement axis and a 1- and 2- directional energy continuum respectively associated with other two dimensions (Fig. 2.1). Quantum dots show a 3-dimensional confinement which makes their electronic state density single atom like, only discrete electronic states are available. The lateral quantum confinement can be used to tune physical properties, such as the band gap. The discrete electron energy spectrum of the quantum dots results in optical spectra with narrow lines (Fig.2.2).

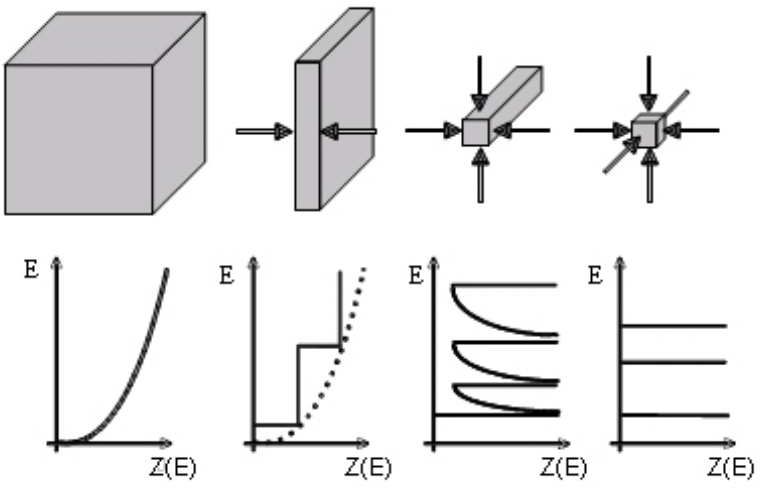


Figure 2.1: Size dependence of electronic density of states. Reduction in size in one or more dimensions cause a discrete energy spectrum.

The broadening of the photoluminescence lines, each belonging to a specific transition, is mainly caused by non uniform size distribution of the quantum dots.

But also more fundamental changes in optical properties can be expected. For example, theoretical investigations of the optical properties of free standing 1-dimensional Si structures predicted a direct band gap characteristic, for an indirect band gap semiconductor (Si) which is diameter dependent [15, 16]. This has been demonstrated in Si nanowires, where a blue shift in the band gap was shown dependent on diameter. The dependence of the optical properties on the diameter of a quantum dot has been also demonstrated for example on colloidal CdS and CdSe quantum dots [2] .

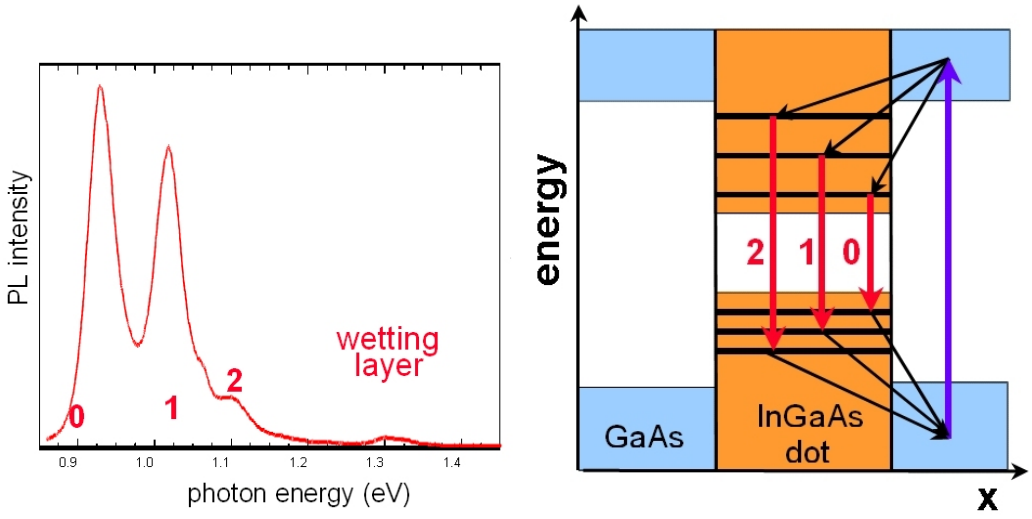


(a) (b)

Figure 2.2: Photoluminescence spectrum (a) and schematic electron states (b) from InGaAs quantum dots embedded in GaAs. Due to 3-d confinement discrete electronic states are established in the quantum dot. The discrete energy transitions result in an optical spectrum with narrow photo luminescence lines. The broadening of the lines is due to the non uniform size distribution of the quantum dots.

## 2.2 Nano structure growth

Currently, two bottom-up approaches for the fabrication of free-standing low dimensional nano structures are exploited: selective area epitaxy [17] (SAE) and metal-catalyst assisted growth through the so-called vapor-liquid-solid (VLS), as discovered over 40 years ago on the micrometric scale [18] and recently "rediscovered" on the nanometric scale. The first method exploits prefabricated or natural irregularities on the substrate surface as starting points for the growth. The latter method relies on the alloying of a metal catalyst (usually Au) nanoparticle with the semiconductor constituent elements, supplied through a vapor phase. The as-formed alloy acts as an initial nucleation site for the material and further guides the nanowire growth. The diameter of the nanowire is correlated to that of the metal nanoparticle [19].

The VLS growth mechanism was first proposed by Wagner and coworkers [18] for semiconductor whiskers growth. The whiskers grown by this mechanism in a Chemical Vapor Deposition (CVD) apparatus were tens of microns in diameter and scaled with the diameter of metal particles used to nucleate the whiskers growth. To produce structures of few nanometers in diameter (< 10nm) and tens of $\mu$m long, precursors leading to a particle size of 4-20nm have

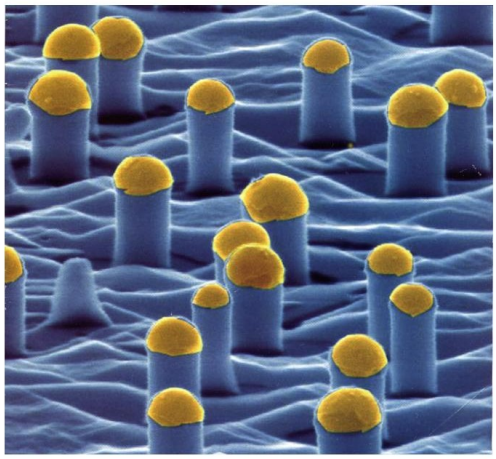

Figure 2.3: SEM image of nano columns grown by VLS with metal-catalyst assistance. Note the gold nano spheres on top of the columns.

been developed. The semiconductor feed stock can come from CVD or laser vaporization. The VLS growth mechanism has successfully been used to fabricate elemental (e.g., Si and Ge), binary (e.g. GaAs) and ternary compounds (e.g. AlGaAs nanowires [20, 21]).

The VLS growth mechanism is a vapor-phase based synthesis method. Among all the vapor-phase methods, VLS is one of the most successful and widely used techniques in synthesizing single crystalline and polycrystalline semiconductor nano-structures in large quantities. In the Pulsed Laser Vaporization procedure, which is considered the most precise and clean to date, the VLS growth mechanism is a three step process: 1) a semiconductor/metal target is ablated by the laser to generate the plume which contains metal rich molecular-clusters of semiconductor/metal and semiconductor vapor. 2) the cluster size develops, absorbing semiconductor vapor and becomes supersaturated. 3) the excess semiconductor then precipitates at the metal particle surface and form the wires.

In summary, a number of synthesis techniques, such as pulsed laser vaporization, chemical vapor deposition , laser-assisted chemical vapor deposition, lithography, sublimation, thermal evaporation, thermal oxidation, chemical and electrochemical processes, nano-channel templates, etc., have been developed to fabricate novel nano structures of semiconductors. So far, chemical vapor deposition, pulsed laser vaporization and chemical vapor deposition are the most widely used synthesis techniques.

# Chapter 3

# Vibrational Properties of Semiconductor nano-structures

Electronic and phonon quantum confinement have been the subject of extensive studies in the past decades. The electronic quantum size effect is mostly detected as a shift of the interband absorption or luminescence peak to higher energies. This is normally observed in quantum wells, quantum wires or in quantum dots. However, here we focus on vibrational properties and size-induced phonon confinement effects.

For 0-dimensional nano-structures there are many systematic experimental investigation of size dependent Raman shifts. In Fig. 3.1 an example of such a study on $TiO_2$ and $SnO_2$ low dimensional crystallites is shown. A large number of such investigations was possible because of the early availability of the samples, especially oxides and colloids (CdS, CdSe). Also in the case of quasi 2-dimensional structures some studies were performed, dealing mainly with the interface modes between different material layers and zone folding effects (e.g. [25]). For quasi 1-dimensional structures, however, not many systematic measurements on phonon confinement size dependence are known. This is maybe because the controllable growth of such nano-structures was not yet available.

Prior to the experimental nano-structure investigations, some pre-

dictions of their vibrational properties had been made (surface vibrations). For bulk materials theoretical calculations became a reliable method of predictions of vibrational frequencies and are indispensable for interpretation of experimental results. Because the crystalline structure of nano-structures is very similar to that of the bulk the calculations for their lattice vibrations are based on methods established for the bulk.

Two classes of theoretical approaches are used for vibrational properties. The more common approach is the matter model as a macroscopic continuum dealing with its dielectric and mechanical properties on the macroscopic scale. Another possibility is the microscopic approach: the atomistic matter model in which interatomic forces are considered. The latter atomistic approach can be based on simple (but reasonable) assumptions for the interatomic potential (empirical potentials, parameters from experiment or other calculations)

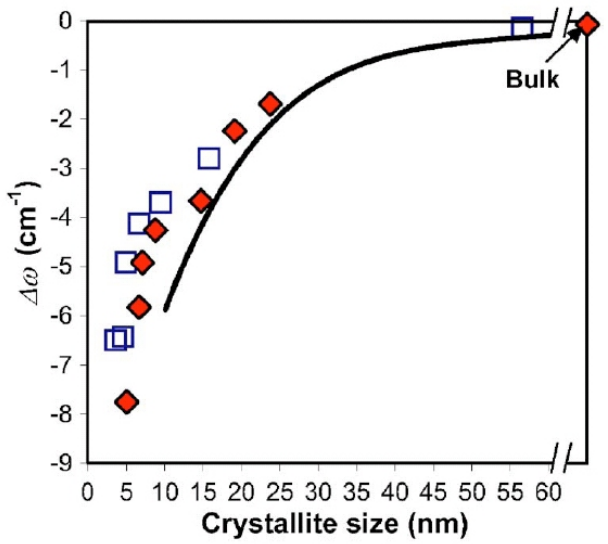


Figure 3.1: Crystallite-size-dependent Raman frequency shift of the $A1_g$ mode relative to bulk frequency. The empty squares represent nano-crystalline rutile $SnO_2$ [22], solid diamonds represent rutile $TiO_2$ Ref.[23], and the solid curve is a phonon confinement model prediction for rutile $SnO_2$ [24] and [22]. Figure taken from Ref.[23].

within the framework of classical Hamiltonian theory (for overview see e.g. in [26]). More sophisticated (and expensive in terms of computational effort) is the consideration of the quantum mechanical nature of interatomic interactions treating the electronic structure (parameter free model, "ab-initio" [26, 27]). In the first part of this chapter some examples on macroscopic and microscopic models for nano-structures will be given in order to describe the potential of modern computational techniques to calculate vibrational frequencies of nano-structures. Moreover a phenomenological model based on known bulk vibrational properties modified by low dimensions arguments will be discussed.

The second part of this chapter is dedicated to the phonon spectral line shapes of nano-structures. A phenomenological line shape model based on the k-relaxation hypothesis will be discussed. The aim of this model is the connection of phonon confinement with the experimentally observed asymmetric line shapes in nano-structures.

Since temperature substantially influences phonon line shapes a treatment of modifications of vibrational properties by thermal effects is indispensable. From the experimental point of view consideration of those effects is crucial since experimental conditions have a strong impact on the temperatures of nano-structures. The effect of an inhomogeneous temperature distribution in nano-structures during the measurements will be discussed. Moreover an anharmonic oscillator model will be presented in order to account for the asymmetric line shapes.

## 3.1 Simple atomic chain model

The 1-dimensional atomic chain is a simple model system for treatment of the collective vibrations (phonons) with simple mechanical equations. The atoms are approximated by masses and the complex interaction between them is simply replaced by spring forces. The

low dimensionality is introduced by means of alternating slices of different materials. The use of periodic boundary conditions (the chain is infinite in one dimension) surely does not reflect the nanometric extent of the nano-structures. A realistic assumption would be a finite structure with either fixed ("clamped") or free outer atoms. The linear chain model contributes to understanding of some important features of phonon confinement. However, though it is a very simplified model, it represents a simple mechanical model known as the mass-and-spring model [28] which considers the interaction of more than the next neighbor atoms. A longstanding discussion if either "free" or "clamped" boundary conditions correctly approximate the vibrations in nano-structures is tackled for instance in Ref.[29]. According to the results in this publication the optical phonons are correctly described by "clamped" boundary conditions while the correct acoustic phonon calculation are subject to free conditions. As far as surface vibrations are considered it is obvious that only free boundary conditions can be used for their calculations since primarily the surface atoms participate to this kind of vibrations.

In Fig.3.2 a linear chain model consisting of materials AB and BC is shown. The simplest approach in order to describe the vibrations in the chain is the consideration of only nearest-neighbor atomic

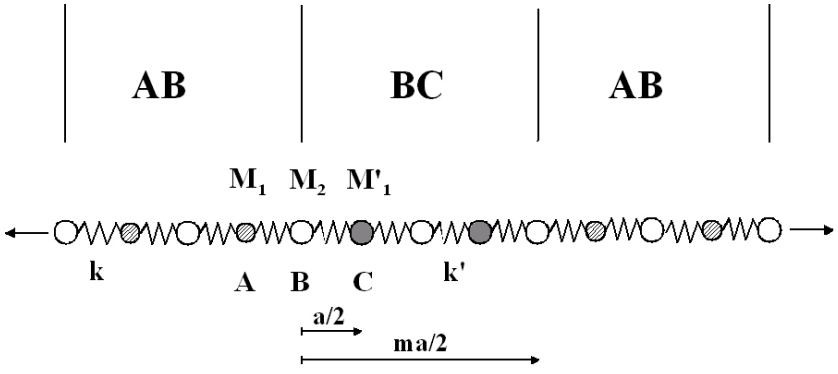


Figure 3.2: 1-dimensional model of alternating layers of materials AB and BC.

interactions, neglecting long range forces. The equations of motion for atoms 1 and 2 in the layer are:

$$M_1 \frac{d^2 U_1(m\frac{a}{2})}{dt^2} = -K\{2U_1(m\frac{a}{2}) - U_2(m\frac{a}{2}) - U_2[(m-1)\frac{a}{2}]\} \tag{3.1}$$

$$M_2 \frac{d^2 U_2(m\frac{a}{2})}{dt^2} = -K\{2U_2(m\frac{a}{2}) - U_1[(m+1)\frac{a}{2}] - U_1(m\frac{a}{2})\} \tag{3.2}$$

where M is the mass of the corresponding atom, $U_i$ is the displacement of the atom *i* along the *z* direction, K is the elastic constant, a/2 is the monolayer thickness and *m* the monolayer number. Solving this equation set (e.g. in [30]) the phonon dispersion relation for the material AB is obtained (Fig.3.3(a)):

$$\cos(k\frac{a}{2}) = \frac{(M_1\omega^2 - 2K)(M_2\omega^2 - 2K) - 2K^2}{2K^2} \tag{3.3}$$

where *k* is the the phonon wave vector. From the calculated dispersion relation the generation of a reduced Brillouin zone is evident with $q_{max} = \frac{\pi}{d}$, smaller than the conventional Brillouin zone with $q_{max} = \frac{\pi}{a}$. Therefore both optical and acoustic phonons are confined within this reduced Brillouin zone.

For a periodic structure made of layered materials AB and BC, acoustic phonons propagate in both materials but their acoustic phonon dispersion branches are folded within the reduced Brillouin zone showing a zigzag-like dispersion relation (Fig.3.3(b)(c)) given by equation 3.4

$$\omega = d(\frac{v_1 v_2}{d_1 v_2 + d_2 v_1})(q + 2\pi\frac{m}{d}), \tag{3.4}$$

where $v_1$ and $v_2$ are the speed of sound in the two media respectively.

Optical phonons also show a well defined confinement within the reduced Brillouin zone, but in this case, optical phonons of the material AB cannot propagate in the adjacent layer of material BC and vice versa. The optical phonon states of AB and BC materials are

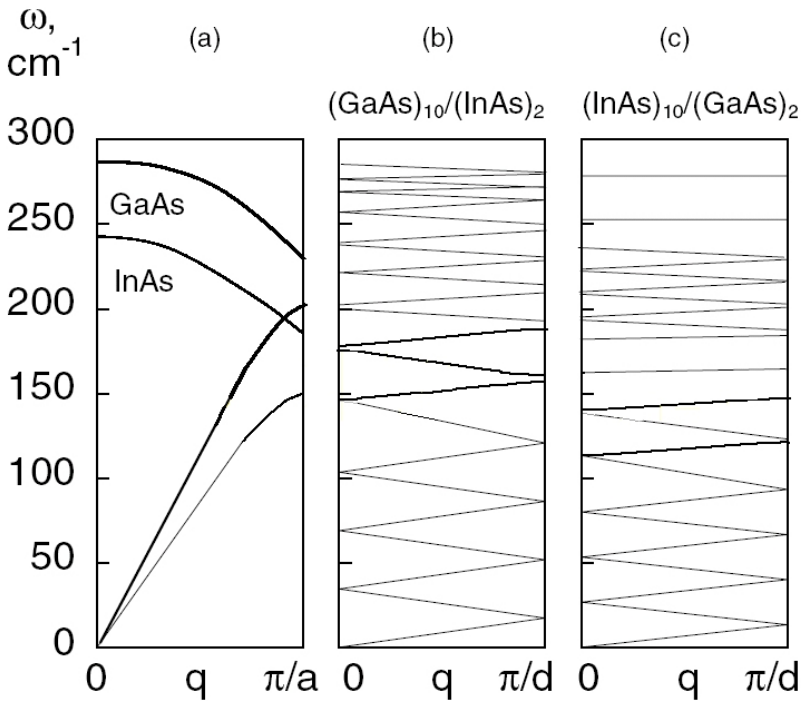


Figure 3.3: (a) Phonon dispersion relation of GaAs and InAs bulk. The reduced Brillouin zone for (b) $(GaAs)_{10}/(InAs)_2$ (c) $(InAs)_{10}/(GaAs)_2$ heterostructures. Figure from Ref.[30].

the forbidden in BC and AB layers respectively because of the different eigen frequency states. The wave amplitude is rapidly damped just after the interface in these materials. Hence a particular optical mode can be represented by a standing wave within the layer (nearly no dispersion occurs in the optical branches). The quantized phonon wave vectors $k_n$ for the two layers can be written as:

$$k_1 = \frac{\pi m}{d_1 + \delta} \qquad \text{and} \qquad k_2 = \frac{\pi m}{d_2 + \delta}$$

where $m$ is the quantum number and $\delta \approx 1$ is the penetration depth.

In Raman spectra of thin layers (quantum wells), lines belonging to interface phonons also appear. These vibrations propagate along the interface and the relationship between phonon frequencies is given

by:

$$\frac{\varepsilon_1(\omega)}{\varepsilon_2(\omega)} = -\frac{d_2}{d_1} \qquad \text{and} \qquad \frac{\varepsilon_1(\omega)}{\varepsilon_2(\omega)} = \frac{d_1}{d_2} \tag{3.5}$$

where $\varepsilon_i(\omega)$ are the dielectric constant of the materials and $d_i$ the layer thicknesses. It is evident that the Raman shift depends strongly on the layer thickness.

Optical and acoustic phonon modes are affected by low dimensionality in a different way. Some acoustic modes are visible as low frequency lines with Raman spectroscopy, but in nano-structures, the LA and TA modes can be folded within the mini Brillouin zone giving a zigzag dispersion relation. Hence, the phonon frequencies appear as several doublet peaks that are relative to the points on folded acoustic branches close to the $\Gamma$-point, still away, however, from the mini-gaps which open at $q_s = \frac{4\pi n}{\lambda}$.

Confinement of optical phonons in a planar layer leads to the appearance of a series of additional peaks at frequencies different from than of the bulk zone center line. Because for the dispersion of optical phonons is negative (for most diamond- and zincblende type materials) the position of confined optical phonons is shifted toward lower frequencies. The frequency shift depends on the size of the nano-structure due to the quantized wave vector which is antiproportional to the size (Eq.3.5). The smaller is the structure the larger are the k values. Intuitively this results in lower frequencies for smaller structures in case of the negative phonon dispersion. The Experimental and theoretical results show that the lower is the size, the higher is the confinement, thus, the higher is the shift to lower wavenumbers.

## 3.2 K-relaxation phenomenological model

Confining a phonon of wave vector $k_0$ in a nano-structure of size L requires the superposition of many bulk phonons covering the range $\Delta k \sim 1/L$. This result is essentially a manifestation of the

uncertainty principle: i.e. $1 \sim \Delta kL$. This range of $\Delta k$ of "activated" phonons should lead to a broadening and shifting of the nano-wire phonon Raman band relative to the band symmetry in the bulk. However, for this effect the phonon mean free path should be larger than the nano-structure size in the propagation direction. For real nano-structures with high numbers of dislocations or impurities this does not need to be the case since this is the limiting factor for the mean free path. It is also limited by strong anharmonic interactions between the phonons leading to shorter lifetimes and therefore smaller mean free paths. To quantitatively understand these changes in Raman activity, schematic phonon bands are shown in Fig.3.4(a) associated with the bulk. Assuming all optical branches as shown are Raman active at the zone center, two Lorentzian Raman lines would be observed for the bulk solid associated with the k = 0 phonons at longitudinal and optical branches. Due to the degeneration of the phonon branches at the $\Gamma$ point (e.g. in elemental semicon-

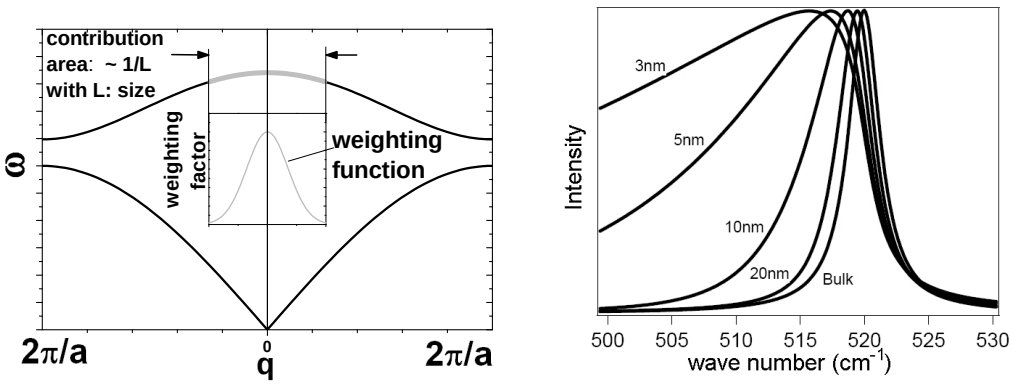


(a) (b)

Figure 3.4: Schematic explanation of contribution to the Raman scattering from the bend phonon dispersion branches due to the k-conservation relaxation. a) Schematic phonon dispersion, the inset represents the Gaussian weighting function for the contributions with different k values around the $\Gamma$ point. b) By k-conservation relaxation model (Eq.3.6) calculated Si phonon line shapes for nano-wires of different diameters. The Si bulk line is shown for comparison.

ductors) only one line would appear in the first-order spectra. In a nano-structure, with diameter L, this selection rule can be broken due to momentum transfer tho the whole structure (in order of 1/L) and phonons around the center of the Brillouin zone contribute to the spectra. The phonon line shape in the spectra depends now on the dispersion of the modes which is mostly either negative (decreasing frequency). A softening and asymmetric broadening to the lower frequencies is expected.

Following this model the quantitative spectra line shape is expected to be a weighted sum over the phonon frequency continuum around the Brillouin zone center. To fit the experimental data a weighting function is introduced in order to describe the assumably different contributions from the $\Gamma$ point and around it. The expression often found in literature [31, 32] is:

$$I(\omega) = \int_0^{2\pi/a} \frac{C(0,k) \quad d^3k}{(\omega - \omega(k))^2 - (\Gamma/2)^2} \tag{3.6}$$

where k is the momentum, $\omega$ is the frequency, $\Gamma$ is the reciprocal phonon life time, $\omega(k)$ is the phonon dispersion relation and $C$ is the weighting function. In many publications the weighting function is assumed to be a Gaussian distribution considering the confinement in one direction (nano-wires) although the original concept [32] is suitable for symmetric (quantum dots) and asymmetric nano-structures with asymmetric confinement (ellipsoids). Functions other than the Gaussian distribution were also taken into consideration (e.g. [23, 33]). In Fig.3.4(b) the phonon line shape calculated by Eq.3.6 is shown. An approximation for the dispersion relation $\omega(k)$ in terms of $(A + B \quad cos(\pi k/2))^{1/2}$ is used with the parameters A,B obtained from fitting the neutron scattering data.

The expression in Eq.3.6 is widely used in order to describe the Raman line shape [33, 34, 35, 36] of nano-structures and to extract the size of the nano-structure by line fits with the size as a fit parameter.

Often it is referred to as the "Phonon confinement model". Attempts were also undertaken in order to explain the second order spectra of nano-structures by this model [37].

It is common in phenomenological theories of nano-structures that bulk properties (crystal structure, phonon dispersion relation, dielectric constants, inter atomic distances) are used in order to explain nano-structure properties. Even though this might be justified for larger nano-structures (>10 nm) where the bulk-like core volume is dominating, smaller nano-structures and the surface effects require other approaches since their properties can differ significantly from that of the bulk.

## 3.3 Continuum models

Simultaneous solution of mechanical continuum equations and Maxwell equations in the electrostatic limit [38, 39] provides phonon dispersion relations for bulk, surface and nano-structures. The advantage of continuum models is that they provide explicit analytical expressions for eigenfrequencies, displacement eigenvectors and Frölich interaction Hamiltonians. The reason for this is the consideration of macroscopic fields which are important for long range interactions. In microscopical mechanical models only short range forces within the interatomic potential are considered. In continuum models the parameters are determined by using bulk properties (phonon dispersion, dielectric constants) assuming that they do not change because of the low dimension. This could be reasonable for nano-structures with sizes above ca. 10 nm, even though nano-structures (in the size range below approx. 3 nm) might have parameters deviating significantly from those of the bulk (eg. phonon dispersion relations [40]).

Rigid and free boundary conditions can be used for the solution of the mechanical and electrostatical differential equations. Either the

mechanical or the electrostatical fields are fixed at the surface of the structures. In the bulk, confined modes are described well by "rigid" boundary conditions, but it is impossible to describe the interface modes because of static conditions on the surface. Under free boundary conditions the continuity of either the mechanical or dielectric fields is not conserved. Relaxation of the rigid boundary conditions has been successfully applied, however leading to good agreement with experimental data.

In polar crystals the longitudinal optical phonons are accompanied by a macroscopic electric field (this field causes zone-center splitting of LO and TO phonon frequencies). Therefore vibrational modes can be calculated within the dielectric continuum model [41] for structures which have a well defined local dielectric constant. An example for such a calculation is shown in Fig.3.5. Significant phonon line shifts with respect to the bulk phonon frequency occur only for small dimensions of the nano-structures (R$< 50$).

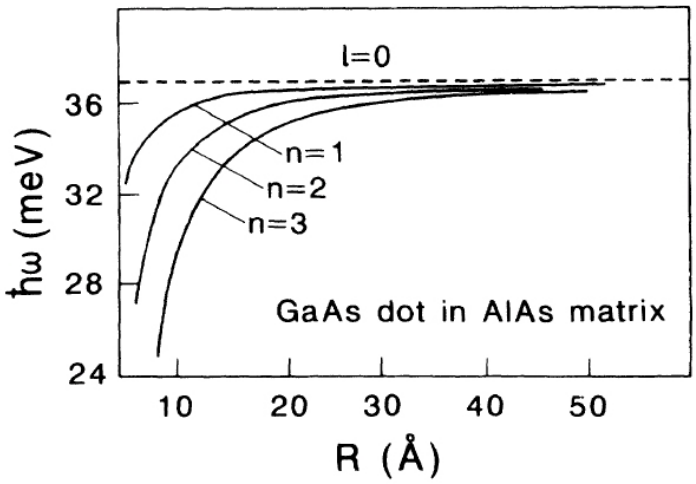


Figure 3.5: Phonon energies as a function of the size of the GaAs quantum dots embedded in an AlAs matrix (from Ref.[39]) calculated by dielectric model. Only the spherical (l=0) modes are shown. The quantized parameter n (from modified Bessel functions in the solution) can be associated with a possible standing wave within the nano-structure.

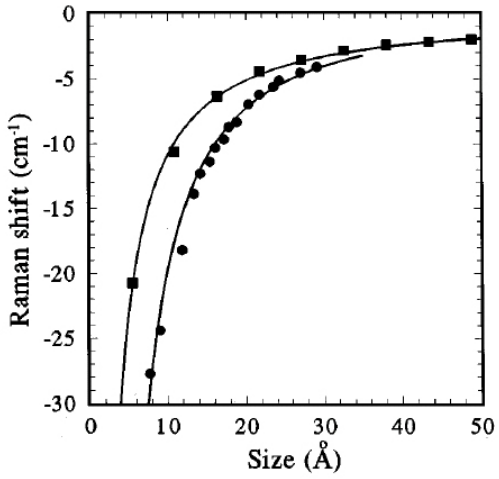


Figure 3.6: Calculated Raman shifts with respect to the frequency of the optical phonons at the zone center. TO phonon of freestanding Si quantum dots (circles) and nanorods (squares) are calculated by partial density approach [46] from [43]. The lines are fits by $\Delta\omega = -A\,(a/L)^{\gamma}$, where *a* is the lattice constant, L is the structure size, *A* and $\gamma$ are the fit parameters.

In wurtzite nano-crystals the phonon modes can differ substantially from those in zincblende nano-crystals due to the uniaxial anisotropy. Therefore anisotropic materials require modifications of the model[42].

## 3.4 Microscopic theories

To simulate a nano-structure within the atomistic approach where the standard periodic condition can not be applied because of the finite size(it can be applied only in non-confined directions) the whole structure has to be modelled. Obviously only very small nano-structures (clusters with few atoms)can be modelled because of large computational effort. However, by applying some approximations (e.g. [29, 43, 44, 45]), a treatment of nano-structures consisting of some hundred atoms seems possible (quantum dots and columns of few nanometer size). Even though the nano-structure size is still limited to a few nanometers such calculations seem to be more reliable from the methodic point of view then by continuum models, especially for small nano-structures (sub-nanometer, nanometer range). In Fig.3.6 phonon frequency calculations performed by the bond polarizability model [47] are shown (from [43]) with force constants calculated by the partial density approach [46]. The size dependency of the

phonon frequencies confirm qualitatively the results from continuum model calculations. The phonon dispersion relation calculated by this more expensive model already appears to be "smeared out" for particle size of about 3 nm in contrast to well defined bulk phonon dispersion relations used for continuum model calculations.

## 3.5 Quantum mechanical model

What previously described models have in common is that they rely on material parameters which have to be used in the calculations. Thus some estimations and assumptions have to be made before the calculations are performed. In principle any reasonable model with a sufficiently large number of parameters can lead to a good fit of the phonon dispersion curves or the phonon line shape.

The ab-initio (also known as first princip) approach is a method that does not rely on parameters from experimental results and is based on quantum-mechanical theory. Instead of modelling the interatomic forces by empirical models a quantum-mechanical problem including all electrons and nuclei has to be solved. This many body problem can be reduced by the Born-Oppenheimer approximation and further simplified by Density Functional Theory (DFT).

In order to determine the vibrational frequencies of the crystal structure two ab-initio approaches are commonly used: the frozen phonon method and the perturbative approach [26]. The basic idea of the frozen phonon method is the calculation of the total energy as a function of the atomic displacements. The force constants can be obtained by differentiating the calculated energy. This energy has to be calculated for displacements of the atoms within a supercell (composed of many unit cells). Large supercells are necessary in order to model the vibrations with displacements which cause a reduction of symmetry. Therefore the application of this method is restricted to high symmetry wave vectors because of high computa-

tional effort for large supercells. The need for large supercells can be avoided by using the perturbative approach [27]. This is based on the fact that the distortions associated with the phonons can be represented by a static perturbation acting on the electronic states.

DFT based approaches have the advantage that the electronic states are treated together with the vibrational properties, since the main application field of DFT and similar approaches are the structural, electronic and optical properties. A "global" treatment of many parallel existing effects can be applied by this theoretical approach. Because of the already mentioned computational effort fields of application in solid state physics are limited mainly to periodic structures (infinite crystals) with a elementary cell containing at maximum only a few hundreds of atoms.

For small nano-structures ($< 2nm$), however, the symmetry is already disturbed by non-infinite boundary conditions. It seems that in this case the whole nano-structure (in case of QD) or a cross section in confined direction (slice of nano-wire or nano-tube) should be modelled.

Only few calculations by this extensive ab-initio model are available up to now, mainly for thin layered quantum well structures (e.g. [48, 49]). It is desirable that more systematic ab-initio calculations of vibrational properties will be performed in the future.

## 3.6 Thermal effects on the phonon line shape

Up to now the changes in phonon frequency of the nano-structures with respect to bulk were discussed. But the phonon line shape parameters like line width and asymmetry also contain information on the vibrational properties. In bulk materials, the broadening of these lines is inversely proportional to the phonon life time. Thus the evaluation of the line widths provides information on the free path length and anharmonic decay processes. Stress and defects in crystals in-

fluence the line shape as well.

The Raman line shape for the bulk can be expressed in a simplified form as [50]

$$I_s(T,\omega) \propto \frac{\Gamma(T)}{(\omega(T)-\omega)^2+\Gamma^2(T)} \tag{3.7}$$

with $\Gamma(T)$ as the half width of the line at the half maximum, given by (following the notation in [51, 52, 53]):

$$2\Gamma_{LO}(T) = A\left[1+n_1+n_2\right] + B\left[1+3n_3+3n_3^2\right], \tag{3.8}$$

where $A+B$ is the LO line width at T = 0 K. $A$ treat the influence of a decay into two phonons while $B$ treats the case of decay into three phonons. The occupation numbers ($n_i$) for the phonons which are involved in the decay process ($\omega_{ac}^i$, $i$=1,2,3) are given by:

$$n_i = \frac{1}{\exp\left(\dfrac{\hbar\omega_{ac}^i}{k_B T}\right)-1}. \tag{3.9}$$

Similarly the frequency shifts can be described with

$$\begin{aligned} \omega(T) &= \omega_0 - \Delta^{(1)}(T) - \Delta^{(2)}(T), \qquad (3.10)\\ \Delta^{(1)}(T) &= \omega_0^{TO,LO}\left(\exp\left(-3\gamma^{TO,LO}(q=0)\int_0^T \alpha(T')dT'\right)-1\right),\\ \Delta^{(2)}(T) &= C\left[1+n_1+n_2\right], \end{aligned}$$

where $\Delta^{(1)}(T)$ is the term describing the line shift through thermal expansion and $\alpha(T)$ is the linear thermal expansion coefficient used for the numerical calculation of $\int_0^T \alpha(T')dT'$. The $\gamma^{LO}(\Gamma)$ and $\gamma^{TO}(\Gamma)$ are the Grüneisen parameters. . $\Delta^{(2)}(T)$ is the energy shift resulting from multiple phonon decays, taking into account the contribution of anharmonicity up to the fourth order, $\omega_0$ is the phonon frequency at T=0 K.

It is clear that the phonon line frequency and line width are temperature dependent. (Fig.3.7). From Eq.3.7 it is also clear that the line

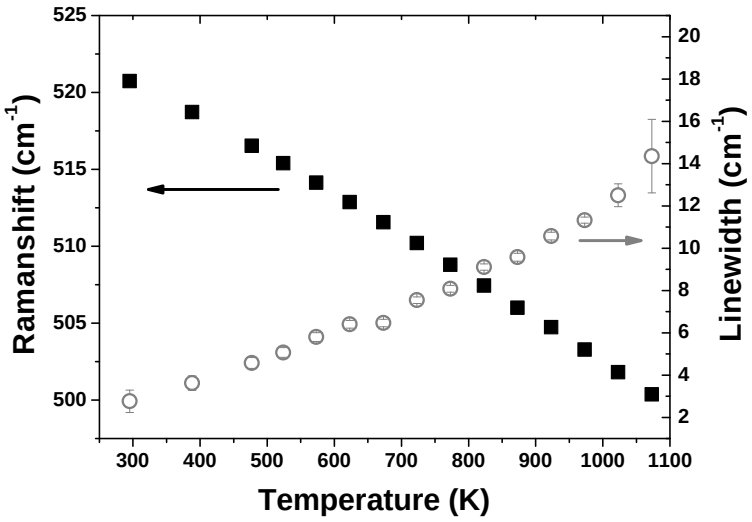


Figure 3.7: Si bulk TO phonon temperature dependent Raman shift (filled squares) and the line width (empty circles).

shape of the bulk phonon line corresponds to a symmetrical Lorentz line.

In Chapter 4.4 measurements on Si and GaAs nano wires will be shown where the line shape of the phonon lines is asymmetric. Of course asymmetric line shapes appear also for bulk materials for example as Fano line shapes [54]. But strong doping and a near resonant laser excitation is required in order to favour the coupling between the phonon states and the electronic continuum. The k-relaxation model (Ch. 3.2) generates an asymmetric line shape. But since the line asymmetry in measurements (Ch. 4.4) changes with the applied laser power the temperature effect has to be considered additionally to the k-relaxation model. There are few proposals to modify the k-relaxation model introducing variable line shifts and widths due to increased temperature temperature. This, however, increases the number of parameters in the model and complicates the interpretation of the results. In the following possible explanations for this phenomena based on the temperature increase of the nano-

structures during the measurement will be given.

Due to the weak cross section for the Raman scattering process, considerable laser power densities are necessary to obtain phonon spectra from nano-structures. The strong focussing of the exciting laser light, necessary for the spatial resolution on the limit of the diffractional optics, increases dramatically the power density ( $10-1000kW/cm^2$). This can lead to heating of the nano-structures with respect to their environment temperatures due to light absorption. Especially in case of strong absorbing materials, much of the laser power is absorbed, while for nano-structures made of transparent materials the influence of the increasing laser power on the spectra shape is not significant (Fig.4.5). Due to the heating, anharmonicity induced effects on the vibrational spectra of absorbing material nano-structures are expected:

- the frequency of the lattice vibrations is reduced according to the lattice expansion and anharmonicity of the crystal potential.
- The lifetime of the phonons is reduced due to the increased number of phonon-phonon interactions because of a higher occupation number (many phonons), leading to the increased line width appearing in the spectra.

These effects have been thoroughly investigated on bulk solids, experimentally as well as theoretically (see above). For bulk solids the illuminated spot is usually much smaller than the sample size. The heat conduction (of course dependant on material heat conduction properties) from the spot into the surrounding material prevents a significant local increase of temperature. In order to observe the above mentioned effects due only to the incident laser beam heating very large power densities are necessary [55]. Nano-structure embedded into or onto bulk matrices (QW, QD or NW on surfaces) do not suffer a dramatic temperature increase, just like in the bulk. In the case of freestanding nano-structures no surrounding bulk material is available. The heat transfer from nano-structure to the bulk is

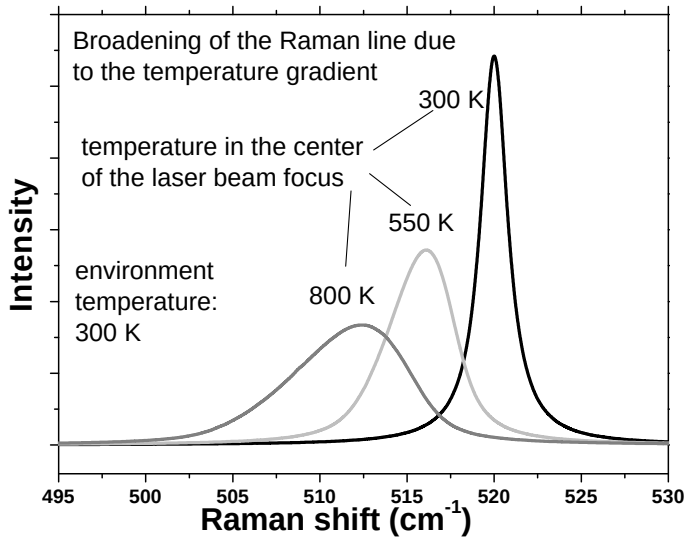


Figure 3.8: Calculated Si nano-wire Raman line shapes at different heating power. The shift and the asymmetric broadening of the lines is due to the non homogeneous temperature distribution within the wire. A gaussian power distribution is assumed within the excitation focus. Assigned temperature values indicate the maximum temperature in the center of the excitation spot. The temperature decreases to 300 K outside of the laser spot.

essentially reduced. The thermal radiation and heat transfer to the surrounding air are not sufficient to compensate laser power heating in order to keep the nano-structure in thermal equilibrium with the environment. Temperature increases of several hundred K can be generated using already comparably low laser power.

### 3.6.1 Inhomogeneous temperature distribution due to the laser spot heating

Inhomogeneous temperature distribution in low dimensional structures may lead to effects on the phonon line shape. Contributions to the signal of different broadening and frequency shifts with respect

to the bulk line shape at room temperature may be expected.

The temperature distribution within the nano-structures that are illuminated and thus heated up by the focused laser light might be inhomogeneous because of two reasons. The power distribution within the laser spot is not uniform but will correspond roughly to the Gaussian function. The second reason is that due to the low dimensions of the nano-structures, reduced heat is transported from the illuminated area to the surrounding media.

Because of approximately Gaussian intensity distribution within the laser focus a similar power density distribution along the nano-wire can be assumed. The resulting line shapes at different laser powers are shown in Fig.(3.8). The lines are asymmetric and shifted to lower wave numbers in respect to the bulk frequency. Thus the asymmetric phonon line shapes from nano-structures might be an effect of the laser heating and inhomogeneous temperature distribution [56]. Especially the Raman line shapes of one dimensional structures, because of their one dimensionality (linear temperature distribution) and comparably weak heat transport due to small cross section, are likely candidates for this explanation.

### 3.6.2 Anharmonic oscillator model

Some experimental (electron microscope holography [57] ) and theoretical [58] results suggest that the internal electrostatic potential inside the nano-structures is not uniform and may show considerable gradients. Therefore the interatomic lattice potential may be superimposed by non uniform electrostatic fields within the nano-structure. If such field gradients exist, a non symmetric distortion will occur in the interatomic potential. In the mechanical picture of the lattice vibration an asymmetric potential causes anharmonic effects. A treatment in terms of mechanical oscillations in an anharmonic potential that is similar to other cases (e.g.[59]) thus seems opportune.

Another argument in favor of dealing with the anharmonicity is the mean free path of the phonons which is anti proportional to the life time (at room temperature in Si bulk this is typically $\sim$7 ps which corresponds to a ca. 100 nm mean free path).

In nano-structures the size is one of the limiting factors for the propagation distance of the phonons since it is of the same order or smaller. The phonon life time is probably reduced, leading to broadening of the phonon line.

To understand the effect of an anharmonic potential on the line shape a simple mechanical oscillation differential equation (Eq.3.11) was solved. To keep the mathematics as simple as possible a one particle oscillation in an anharmonic potential was treated. The first term is the inertial force, the second term is the force from the potential, dependent on the deflection r, whereas the energy dissipation is considered in the third term, which is proportional to the "velocity" of

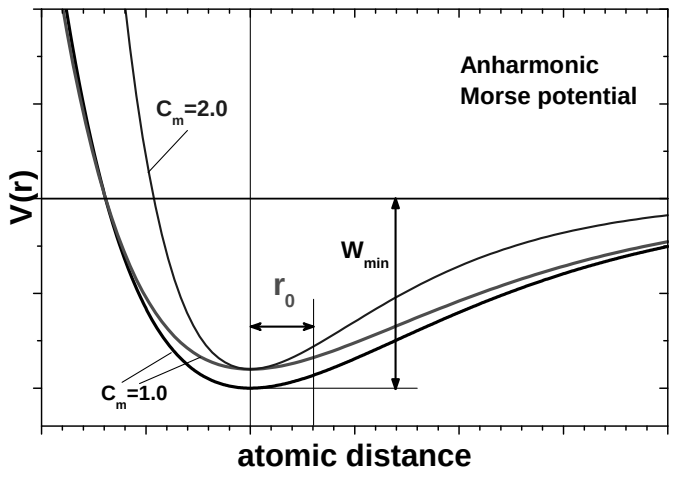


Figure 3.9: Morse potential ad its parameter dependent behavior. $C_m$ determines the asymmetry of the potential. $W_{min}$ determine the potential barrier and is independent from $C_m$. $r_0$ is the initial oscillation amplitude and is not a potential parameter but it is defined with respect to the potential minimum.

(a)

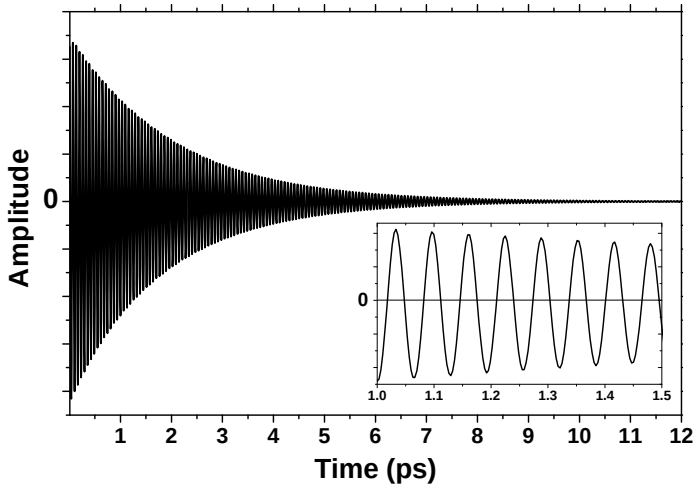


(b)

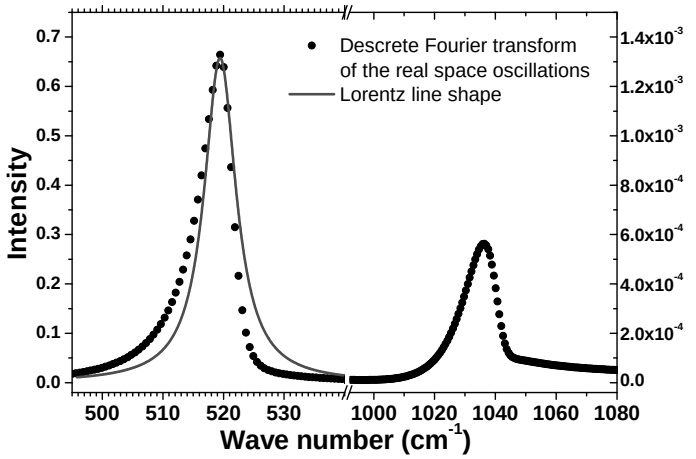


Figure 3.10: Calculation of line shapes by the anharmonic oscillator model. (a) Calculated real space vibrations. Slightly asymmetric amplitude and amplitude decay appear due to asymmetric potential and damping. In the magnified inset the quasi sinus shaped form of the vibrations is recognizable. (b) Comparison of the discrete Fourier transform of the real space vibrations in (a) and the Lorentz line shape. Due to anharmonicity also the second harmonic vibration appears in the range of 1040 $cm^{-1}$.

the particle.

$$M\left(\frac{\delta^2}{\delta t^2}r(t)\right) + \frac{\delta}{\delta r}V(r) + R\left(\frac{\delta}{\delta t}r(t)\right) = 0 \qquad (3.11)$$

To describe the anharmonicity of the studied system, for many calculations the Morse potential is applied (Eq.3.12). The asymmetry of the potential can be controlled by changing the anharmonicity factor $C_m$. The depth of the potential is expressed trough $W_m$. A very useful feature of the Morse potential is the fact that the variables $C_m$ and $W_m$ are independent. It means that the variation of the potential depth does not distort the potential asymmetry.

$$V(r) = W_m \left(1 - e^{C_m(r-d)}\right)^2 + W_m \tag{3.12}$$

The qualitative behavior of the Morse potential according to its parameters is shown in Fig.3.9.

The time dependent amplitude of the damped oscillation is calculated numerically in real space using the following boundary conditions:

$$\frac{\delta}{\delta t} r(0) = 0; \qquad r(0) = 0 \tag{3.13}$$

A numerical solution algorithm using a Fehlberg fourth order Runge-Kutta method with degree four interpolant proved to be reasonable in terms of accuracy and calculation time.

The Fourier transform of the real space vibrations yields the frequency spectra of the calculated vibration. Five parameters in total are used in this model: $r_0$ - initial amplitude, M - particle mass, R - dissipation factor, $W_m$ - potential depth, $C_m$ - potential anharmonicity.

The parameter of the Morse potential can be interpreted in terms of modelled system physical properties:

- Due to the increase of temperature the atomic distance increases leading to the increase of the potential depth $W_m$.
- The initial amplitude of the atomic vibration $r_0$ increases (higher vibration energy in classical picture).

- Because of the higher phonon occupation number the interaction between the phonons leads, in classical picture, to faster energy dissipation, and hence, an increase of the dissipation R.

It seems to be reasonable that by using these parameters a temperature dependent behavior of the oscillation can be simulated. The influence of the parameters $W_m$, $r_0$ and R on the calculated line shape is shown in Fig.3.11. As expected, by increasing the dissipation factor (damping constant in the differential equation 3.11) the intensity decreases and the line is only slightly symmetrically broadened. Increasing the potential depth $W_m$ increases the force applied to the oscillating particle and therefore increases only the oscillation frequency. The initial amplitude $r_0$ causes the most interesting effect on the line shape. It broadens the line asymmetrically and it even causes a splitting of the line for high initial amplitudes. To fit the parameters for the asymmetric line shapes from an experiment the symmetric line of the bulk phonon is fitted first. Keeping fixed all the other parameters (potential asymmetry and particle mass) the three parameters $W_m$, $R$, $r_0$ are then changed in order to fit the asymmetric lines shapes of the nano-wires.

This very simple model was successfully applied for fitting the temperature dependent Raman line shapes of Si nano-wires in Ch.4.4. The parameters $W_m$, $R$, $r_0$ were changed in agreement with the increased temperature: potential depths $W_m$ were increased, the dissipation factor was increased as well as the starting oscillation amplitude $r_0$. In spite of the model (a simple one particle oscillation in an anharmonic potential) the fits are promising. Though the numerical values of the fit parameter are meaningless the qualitative trends strengthen the hypothesis that the crystal anharmonicity in connection with the increased temperature may cause an asymmetric line shape of nanostructures.

(a)

(b)

(c)

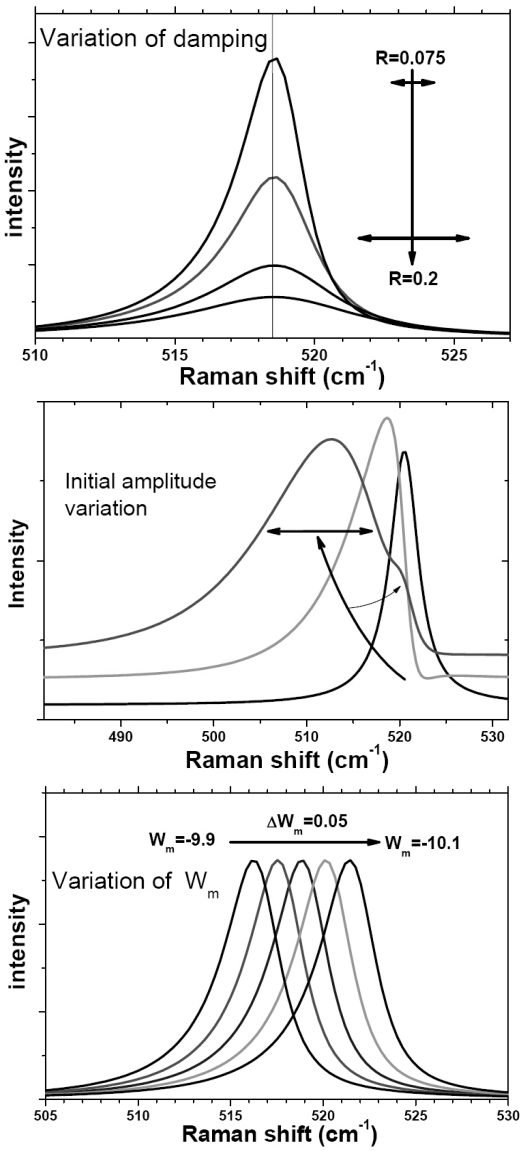


Figure 3.11: Calculation of line shapes by the anharmonic oscillator model. Dependency of the line shape on model parameter is shown by variation of a single parameter. (a) By variation of damping parameter R mainly the intensity is affected. (b) The initial oscillation amplitude $r_0$ influences the broadening. (c) The frequency shift of the line depends on the potential depth $W_m$.

# Chapter 4

# Micro Raman Measurements from Semiconductor nano-structures

In Micro-Raman the diffraction limited spatial resolution of several 100 nm is best approximated by a confocal optical microscope [60]. Despite recent developments of methods beyond the diffraction limit (Ch.5) this is still the most widely used technique for high spatial resolution spectroscopy. By using pinholes in the image planes of the microscope lens the diffraction fringes are suppressed and the lateral resolution improves by a factor of about $\sqrt{2}$ at best. A technical realization of a confocal microscope for use in microscopy spectroscopy is shown in parts of Fig. 6.1.

First, in this chapter measurements with diffraction limited spatial resolution (Fraunhofer) called ***Micro-Raman*** scattering will be shown. In the next chapter the development of the near field spatial resolution Raman scattering set-up (the so called ***Nano-Raman*** scattering) will be presented.

The illuminated region in general includes several nano-structures being randomly distributed and oriented due to the growth procedures (Fig. 4.1). In general the nano-structures in the laser focus will have different properties due to size, shape and orientation (Fig.4.1b). Deriving well defined properties of single nano-structures by means of measurement averaging over several different

structures is therefore difficult. Even if a single nano-structure can be isolated the entire nano-structure will contribute to the signal. Hence its internal structure e.g. hetero-junctions or inhomogeneities (defects, stoichiometry) still remain indistinguishable. Furthermore, only a small part of the laser light excites the nano-sample. Thus severe intensity and signal-to-noise ratio problems in single nano-structure measurements might be encounted. Consequently micro-Raman has been applied up to now mainly to nano-materials with a large Raman cross section.

In spite of these drawbacks, information on the phonon frequencies can still be extracted and quite a large number of data have been published. This concerns first of all data on carbon nanotubes [61, 62, 63, 64, 65]. We present in this section some examples performed on the 1-d nano-structures shown in Fig.4.1. As indicated by the white circles, which indicate micro-Raman spatial resolution, the spectra represent averages over several nano-structures.

## 4.1 Raman scattering

There exist many reviews on Raman scattering in solids dealing with the basic features of this process which includes two photons (incident and scattered) and an elementary excitation of the solid [25, 66, 67]. Resonant phenomena, especially important for nano-structures with their small scattering volume, have been treated in Ref. [68, 69]. The basic features of Raman scattering from vibrational excitations in nano-structures are similar to those of the bulk and independent of the dimensionality of the system. This concerns the experimental techniques, the kind of selection rules, resonance phenomena and other properties. For this reason we will confine this section mainly to a short summary of these general properties as they have been discussed in several reviews dealing with bulk systems [67, 68, 69]. We will point out the modifications occurring in

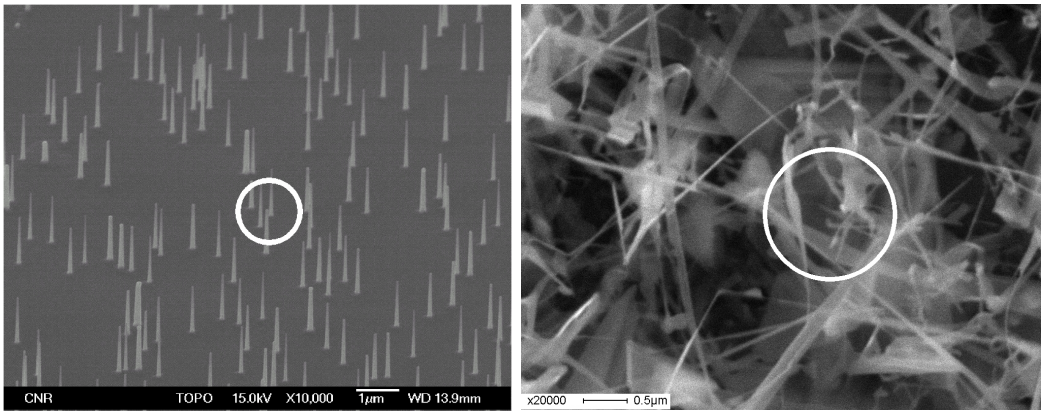


(a) (b)

Figure 4.1: Nanosamples from which spectra are shown in this section. The white circles represent the spatial resolution of the micro-setup: (a) GaAs nano-rods grown on a GaAs(111) substrate by the VLS growth process [20]. The diameter of the nano-rods ( 60nm) corresponds essentially to the size of the gold nano-droplets deposited on the substrate for nucleation purposes. (b)- ZnO nano-wires grown by thermal evaporation. The size and the shape of the nano-structures vary in a wide range dependent on the position on the sample.

lower dimensional systems.

The main difference between Raman scattering from bulk systems and lower dimensional systems is that the latter have electronic states and vibrational properties different from the bulk. While these differences do not cause any principal limitations, the small number of atoms present in the lower dimensional systems turns out to be the main experimental obstacle. As a result the scattering intensities are low and the experiment needs to be carefully designed. Besides standard optical measures such as high aperture, optimized collecting optics for the scattered light between the sample preparation chamber and the monochromator, it turns out that the main advantage comes from the exploitation of cross sectional resonance enhancements (Resonance Raman Scattering). For this reason previous knowledge about the electronic band structure is extremely helpful and quite often the choice of photon energies is the decisive

parameter for a successful experiment. Vice versa, the experiment, which first of all is supposed to determine vibrational properties, allows also to gain information about the electronic states by using different laser lines for excitation.

In the Raman scattering process a certain amount of energy is gained or lost by an incident photon with energy $\hbar\omega_i$ (*incident*) in order to create or annihilate elementary excitations of the solid, usually phonons, resulting in a scattered photon of a different energy $\hbar\omega_s$ (*scattered*). The amount of energy transferred corresponds to the eigenenergy $\hbar\omega_j$ of the elementary excitation involved labeled by "$j$":

$$\hbar\omega_s = \hbar\omega_i \pm \hbar\omega_j. \tag{4.1}$$

Here the "minus" sign stands for a phonon excitation (Stokes process) while the "plus" sign implies a phonon annihilation (anti-Stokes process).

The momentum $\vec{k}_j$ transferred to the vibrational excitation is related to the momentum of the incident $\vec{k}_i$ and scattered light $\vec{k}_s$ according to:

$$\hbar\vec{k}_s = \hbar\vec{k}_i \pm \hbar\vec{k}_j. \tag{4.2}$$

It is quite small in periodic structures when compared to the maximum possible quasi-momentum at the edge of the Brillouin Zone. Thus one usually assumes $\hbar\vec{k}_j \approx 0$. In low dimensional solids, when the periodicity is reduced in one or more directions, the momentum conservation is of course relaxed in the reduced dimensions because the wave vector is not a good quantum number any more. Instead one should discuss the phonons in those directions as confined modes. From the theoretical side however not much has been published in that respect except for the 2-dimensional superlattices [25, 70].

Of course the scattering intensity is experimentally important. This can be expressed as dipole radiation using a generalized dielectric

susceptibility $\tilde{\chi}(\omega_i, \omega_s)$ which is also often called Raman tensor [71]:

$$I_s = I_i \frac{\omega_s^4 V}{(4\pi\epsilon\epsilon_0)^2 c_0^4} |\vec{e}_s \epsilon_0 \tilde{\chi}(\omega_i, \omega_s) \vec{e}_i|^2 \tag{4.3}$$

where $I_i$, $I_s$ and $\vec{e}_i$, $\vec{e}_s$ denote the intensity and polarization, respectively of incident and scattered light.

In a microscopic quantum mechanical approach the generalized susceptibility may be described using time-dependent perturbation theory [66]. The dominant term amounts to [72]:

$$\chi_{\alpha,\beta}(\omega_i, \omega_s) \;=\; \frac{e^2}{m_0^2 \cdot \omega_s^2 \cdot V} \sum_{e,e'} \frac{\langle 0|p_\alpha|e'\rangle\langle e'|H_{E-L}|e\rangle\langle e|p_\beta|0\rangle}{(E_{e'} - \hbar\omega_s)(E_e - \hbar\omega_i)} \tag{4.4}$$

where $m_0$ is the electron mass, $V$ the scattering volume, $p_\alpha$, $p_\beta$ the Cartesian components of the momentum operators, $E_e$, $E_{e'}$ the energies of the excited electron-hole pair states and $H_{E-L}$ the electron-phonon interaction Hamiltonian.

Eq. (4.4) includes the transition from the ground state $|0\rangle$ to an excited electronic state $|e\rangle$ (photon absorption), scattering of the generated electron-hole pair into another state $|e'\rangle$ via electron-lattice interaction, and finally the transition back to the electronic ground state $|0\rangle$ under photon emission.

The first important feature of these two equations is that they describe scattering selection rules. In Eq. (4.3)certain tensor components of the generalized dielectric susceptibility $\tilde{\chi}(\omega_i, \omega_s)$ are selected by the polarisation unit vectors $\vec{e}_i$, $\vec{e}_s$ of the light fields. From Eq. (4.4)they are less visible but contained in the dipole matrix elements. Secondly in Eq. (4.4) the brackets in the nominator shows that the intensity can be strongly increased when the photon energies match the transition energies of electron-hole pair states. Thus for a given material with given electronic states the choice of laser line energy for the scattering experiment is one of the most important parameters. In the following we describe how Raman scattering measurements on nano-structures can be performed.

## 4.2 Micro-Raman spectra on 2-dimensional structures (QW)

The larger penetration depth of light allows to reach regions below the surface which are not accessible by the other surface techniques. Thus Raman scattering can give information on buried layers or interfaces below the surface. The following example of GaAsN layers within a GaAs matrix demonstrates the detection of such vibrations. GaAsN (as well as GaInAsN) with a low nitrogen content is a technologically very interesting ternary material since the addition of N into GaAs reduces the band gap and makes it a potential candidate for IR optoelectronic and solar cell applications [73, 74]. It has, moreover, the advantage that one can use the established GaAs technology. The main experimental challenge is to introduce sufficient quantities of nitrogen into GaAs and also to determine the amount and distribution incorporated. Epitaxial growth of GaAsN has been done by either MBE [75] or MOCVD [76]. In Fig. 4.2 we show Raman spectra of two different GaAsN/GaAs layer structures grown by MOVPE with two different carrier gases ($N_2$ and $H_2$) but with nearly identical nitrogen content (4.8% as determined by X-ray diffraction). Besides the LO(GaAs), new modes labeled LO(Ga-N) and LO(Ga-As), appear in the Raman spectra. While the LO(GaAs) is generated within the GaAs spacing layers or/and the substrate, the LO(Ga-N) has been shown by ion implantation of nitrogen isotopes and IR absorption measurements to be local vibrations of Ga-N bonds [77]. In the presence of such Ga-N bonds, which are shorter than the Ga-As bonds, the lower frequency LO(Ga-As) can also be explained through dilation of the surrounding GaAs leading to a lower frequency than the LO(GaAs) [78, 79]. The occurrence of the two modes thus shows that the nitrogen is not homogeneously distributed in the GaAsN layers, and formation of Ga-N clusters occurs. The appearance of the TO phonon which, in the scattering configuration shown, is forbidden by zincblende symmetry selection rules

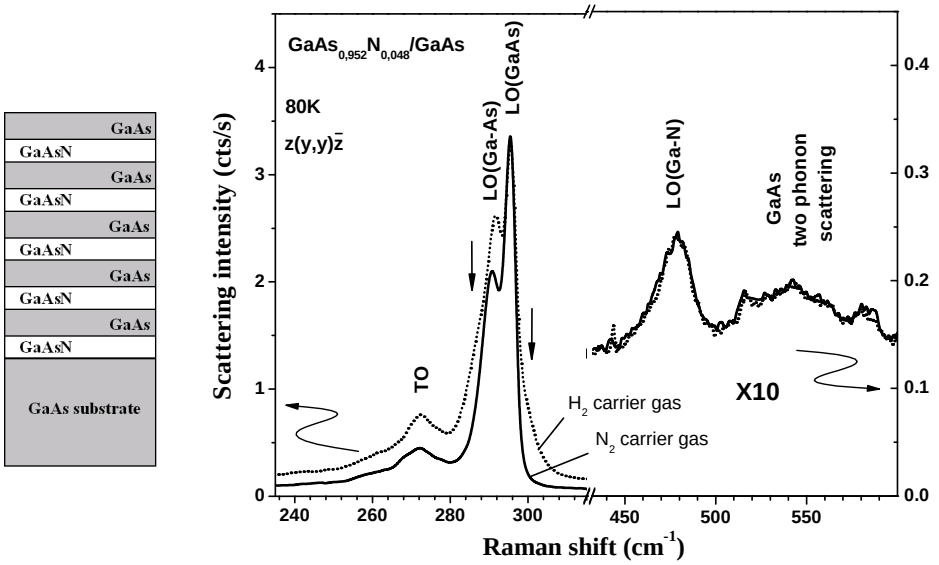


(a) (b)

Figure 4.2: Determination of vibrational properties in "buried" structures. (a) Schematic cross section of MOVPE grown GaAsN/GaAs layer structure with ca. 5.5 nm GaAsN and ca. 9 nm GaAs layer thicknesses. The molar N content within the GaAsN layers in both samples is ca. 4.8% (b) Raman spectra of two similar GaAsN/GaAs layer structures grown with $N_2$ (black curve) and $H_2$ (grey curve) as carrier gas. Additional phonon lines appear at the positions marked by arrow in the spectra of the sample grown in $H_2$ carrier gas (see Fig. 4.3 for details).

proves similar, that the inhomogeneous inclusion of nitrogen disturbs additionally the zincblende symmetry and leads to a disorder in the sample.

In spite of having a very similar structure and a nearly identical stoichiometry, the Raman spectra in Fig. 4.2 of the two samples show a clear difference at the positions marked by the vertical arrows. We therefore undertook a line fit analysis of the $H_2$-carrier-gas-sample Raman spectrum (upper spectrum, dotted curve) with a Voigt line shape. The mathematical procedure results from the convolution

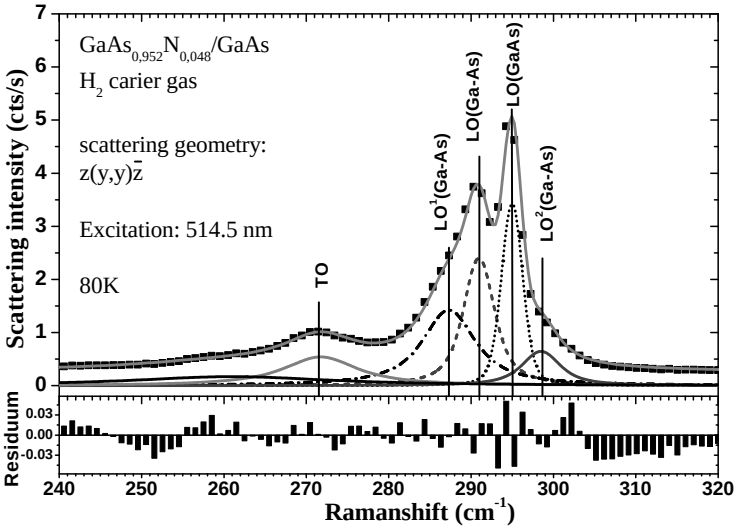


Figure 4.3: Line analysis of a Raman spectra from MOVPE grown GaAsN/GaAs (already shown in Fig. 4.2). Compared to another spectra (with $N_2$ carrier gas Fig.4.2) additional lines appear between TO and LO(Ga-As) and above LO(GaAs). The residuum for the shown fit (difference between measured data and fit function) is displayed in the lower part of the graph.

of a Lorentzian line shape (phonon) with the instrumental Gaussian broadening (monochromator) and is given by [80]:

$$V(\omega) = A_0 + A^2 \frac{2\ln 2}{\pi^{\frac{3}{2}}} \frac{\sigma_L}{\sigma_G^2} \int_{-\infty}^{\infty} \frac{\exp -\omega'^2}{\left(\sqrt{\ln 2}\frac{\sigma_L}{\sigma_G}\right)^2 + \left(\sqrt{4\ln 2}\frac{\omega-\omega_0}{\sigma_G} - \omega'\right)^2} d\omega'. \quad (4.5)$$

with $\sigma_G$, $\sigma_L$ being the FWHM of the Gaussian and Lorentzian lines and $\omega_0$ the peak position. This procedure is well known also in many other spectral analysis techniques. The detailed result of the fit is shown in Fig. 4.3. The accuracy of the fit can be judged from the residuum (shown in the bottom of Fig. 4.3). Since this has no peak structure and only very small values (below 1 %) the two additional phonon lines $LO^1$(Ga-As), $LO^2$(Ga-As) appearing at the positions previously marked by arrows in Fig. 4.2 are significant.

The appearance of additional lines in this sample with the same stoichiometry might look surprising at first glance. However, as discussed before in connection with LO(Ga-As) and LO(Ga-N), this probably originates from different distributions of Ga-N clusters. Even though the average macroscopic concentration is the same, the distribution of inhomogeneities are different and create on a mesoscopic scale additional LO(Ga-As) peaks arising from differently expanded GaAs regions (left side of LO(GaAs)) or compressed GaAs regions very near the Ga-N clusters (right side of LO(GaAs)). Moreover, the higher intensity of the symmetry forbidden TO in the $H_2$-grown-sample confirms the larger disorder.

In conclusion, for the two MOVPE samples grown under different carrier gases it can be stated that the $H_2$-carrier gas sample contains more inhomogeneities than the $N_2$-carrier gas sample. A possible explanation for this are different growth temperatures at the surface caused by the different thermal conductivities of the two carrier gases [81].

## 4.3 Micro-Raman spectra of 1-dimensional structures

Semiconducting ZnO nano-wires where prepared in the laboratories of IMEM Parma by thermal evaporation inside a tubular reactor with controlled gas flow. ZnO nano-wires of different shapes where obtained with thicknesses between 20 and 200 nm (Fig.4.1b). Raman measurements presented here (Fig.4.4) were performed under non-resonant conditions (photon energy$= 2.7eV << E_g = 3.4eV$). Thus the absorbance of the material is very low and higher excitation laser power densities (up to 70 mW/$\mu m^2$) could be applied without the risk of heating effects.

The Raman spectra of ZnO nano-wires (<100 nm diameter) show a clear difference in comparison to the ZnO bulk spectra. From the measurements on the sample in Fig. 4.1b) two different types of

(a)

(b)

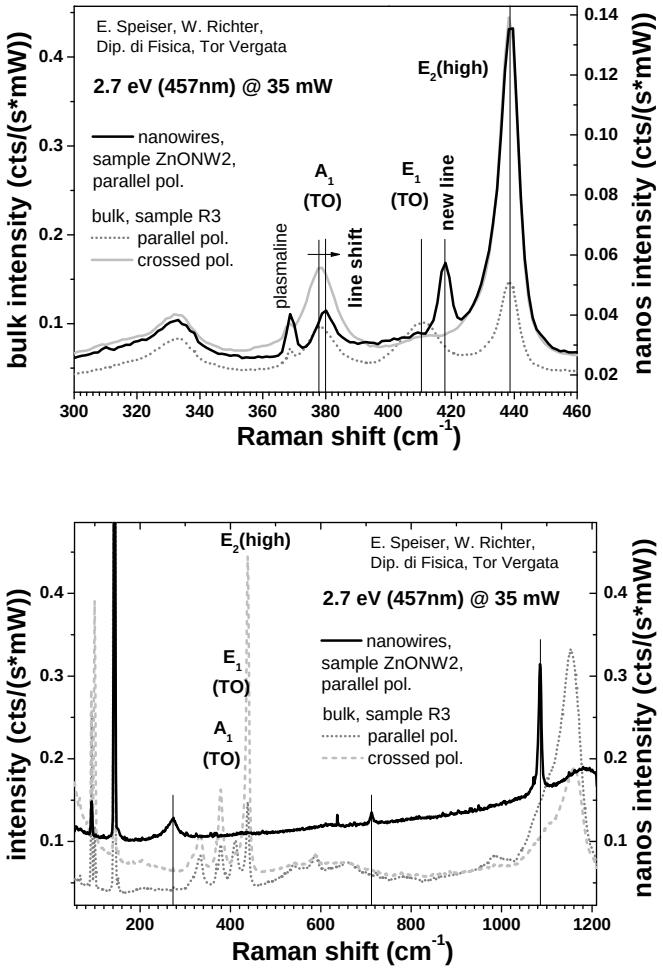


Figure 4.4: Raman spectra of ZnO nano-wires at different positions on the sample (Fig. 4.1b))in comparison to ZnO bulk spectra. (a) Type 1 spectra appear from the central region of the sample. A new line appears in the gap between the $E_1$(TO) and $E_2$ at approx. the 418 $cm^{-1}$. Moreover the $A_1$(TO) line is shifted by ca. 2 $cm^{-1}$ to higher wave numbers. (b) Type 2 spectra appearing on the borders of the sample. Only the double phonon lines seem to contribute significantly to the Raman signal. A narrow intense double phonon line appears at ca. 1100 $cm^{-1}$.

spectra were obtained. They are shown in Fig.4.4a) (type 1) and Fig.4.4b) (type 2). The shown spectra were conformed to be reproducible at different locations on the sample. Type 1 (Fig. 4.4a)

shows the spectra which result from the central region of this specific sample. Type 2 spectra were measured on the border region of the sample. The two graphs are shown in comparison to ZnO bulk spectra. In the type 1 spectra a new line appears in the gap between the $E_1$(TO) and $E_2$ and always at the same frequency. Moreover, the $A_1$(TO) line is shifted to higher wave numbers. Even though this shift seems to be small it has a significant value of approx. 2 $cm^{-1}$ and can not be a result of possible calibration inaccuracy due to direct comparison of the line energies of other lines ($E_2$ and the double phonon line at 343 $cm^{-1}$). According to the bulk phonon dispersion relation of ZnO [82], the new lines or the line shifts could be the result of folded optical phonon branches in the directions from the $\Gamma$ point to the points A, M or K in the BZ.

The type 2 spectra (Fig. 4.4b)) are very different from the previous ones and the ZnO bulk spectra. Only the double phonon lines seem to contribute significantly to the Raman signal. The appearance of the narrow intensive 2LO line at approx. 1100 $cm^{-1}$ suggests the presence of a phonon selection mechanism, for example, because of the small size (confinement) combined with an asymmetric shape of the nano-structure (phonon k-vector selection). The fact that two different types of spectra originate from the same sample is probably due to the slightly different growth condition in its center and on its borders, resulting in nano-structures of different sizes and types.

The appearance of two types of Raman spectra demonstrate the need for higher spatial resolution. Measuring the spectra from a single nano-structure and at the same time its topography would simplify considerably the interpretation of the obtained data.

## 4.4 Thermal effects

The vibrational modes of the nano-structures embedded in bulk materials (quantum wells or quantum dot stacks) or deposited on sur-

faces interact with the bulk vibrational modes. Free standing low dimensional structures like nano-rods or nanotubes offer perhaps a cleaner means for studying confinement in low dimensional structures. The goal is consequently to study the frequency and line shape of the phonons as a function of the size and possibly also the shape of the nano-structures and comparison to the bulk values.

One of the experimental problems in Raman scattering from free standing nano-structures is the thermal management of the incident laser power within the individual nano-structure since the thermal conductance via the surrounding material is largely reduced. Thus the exciting laser power may easily create non-equilibrium conditions. This situation occurs especially in absorbing materials like Si nano-wires. Such conditions have been already discussed for Raman scattering in Si bulk under the aspect of laser crystallization [55]. For transparent materials (large band gap) these effects, however, are not important because the laser power absorbance by the nano-structures is not significant. Laser power normalized Raman spectra of $SnO_2$ nano-wires (average diameter ca. 200 nm) at different excitation power are shown in Fig.4.5. In spite of high laser power density up to $70mW/\mu m^2$ no changes in the spectra appear.

In contrast to this observation the materials with lower band gap energies absorb significant amounts of the laser power. In Fig.4.6 the Stokes and anti-Stokes line of a single Si nano-wire at an excitation laser power of 1 mW is shown. The Raman frequency of the Si TO phonon is significantly lower than the bulk frequency at room temperature ($520.7 \quad cm^{-1}$). From this measurement the temperature increase can be estimated by the Stokes/Anti-Stokes intensity ratio and the frequency shift using the bulk phonon frequency temperature dependence (Fig.3.7 and Eq.3.10). The temperature induced frequency shift of $\Delta\omega = 17cm^{-1}$ estimated from Fig.4.6 corresponds to a temperature of ca. 900 K. By evaluating the Stokes/Anti-Stokes intensity ratio (using sensitivity corrected intensities) a temperature of ca. 560 K is obtained. This discrepancy may be explained by

the fact that the line shapes are distorted (asymmetry and a shoulder at the higher frequency side). One possible interpretation is a non homogeneous temperature distribution (Ch.3.6.1). Lower temperature regions of the nano-structure is represented by the higher frequency peak and the higher temperature regions are represented by the lower frequency shoulder. By splitting the phonon line in to different contributions the evaluation of the intensity ratios became meaningless (evaluation of line areas instead of intensities could resolve this problem). In this case the estimation of the temperature by the frequency shift seems to be more reliable. However, a drastic temperature increase of several hundred K occurs in the nano-wire by laser spot heating.

The temperature increase induced by the laser depends on many parameters (laser power, thermal conductivity, heat capacity of the sample, thermal radiation) and is difficult to control. Moreover, even with a micro Raman setup the focus ( $\sim 1\mu m$) on a sample similar to that shown in Fig. 4.1a will cover an area containing several Si nano-wires which possibly might also have different geometries.

The experimental solution to this problems is the measurement of spectra with different laser powers on a single nano-structure. Nano-wires scratched from the growth substrate surface were deposited on glass surface. Single nano-wires were selected by eye and placed within the focus of the laser beam using a micrometric table. During the alignment of the structure within the laser focus low laser power was applied in order not to damage the sample by melting it. The average diameter of the nano-wires used for the experiment shown in Fig. 4.7 was previously determined by scanning electron microscopy to be in the range of 150 nm. Thus it can still be identified by an optical microscope even though no exact values can be given for its diameter due to the optical resolution limit.

In Fig. 4.7 the scattering intensity has been normalized to the incident laser power. The Si-nano-wire phonon shows a strong shift to

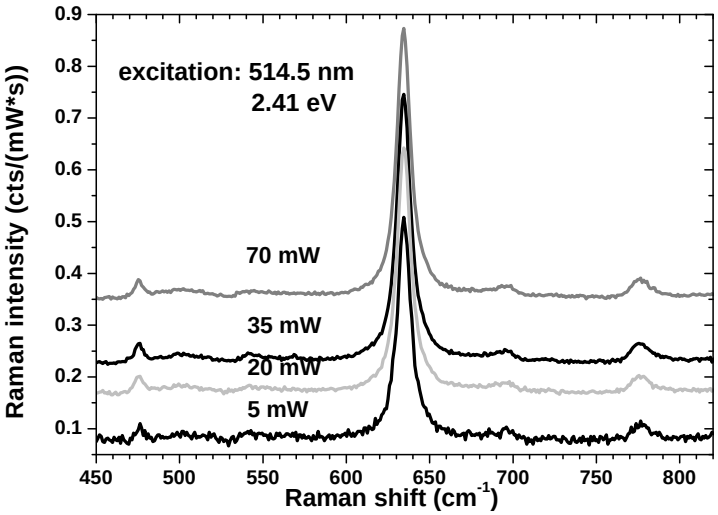


Figure 4.5: Raman spectra of $SnO_2$ nano-wires (diameter ca. 150 nm) at different excitation laser power. No significant changes in the spectra are observed due to laser power increase.

lower wave numbers and an asymmetric broadening with increasing laser power similar to those reported in Ref. [56, 83]. The extrapolation to zero power gives no significant differences to the Si bulk frequency, thus no confinement effect is observed. It is, however, not expected in nano-structures of the size above 100 nm.

The line asymmetry observed in Fig. 4.7 is usually discussed in terms of the geometrical boundaries in the low dimensional particles which as a consequence lead to an extended range of k vectors in reciprocal space (relaxation of k conservation). The Raman line shape is then obtained by the weighted integration across the phonon dispersion curves (Ch. 3.2). However, the line asymmetry in Fig 4.7 disappears for low excitation power. This shows that the asymmetry of nano-structure Raman lines can not always be described by simple relaxation of k vector conservation. The strong asymmetric broadening was also observed for Si bulk at high temperature [84]. Thus for nano-structures it could possibly result from the anharmonicity

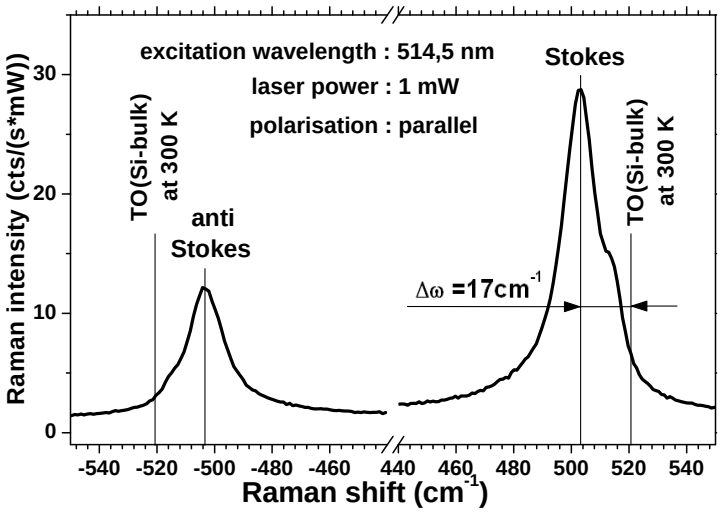


Figure 4.6: Stokes and anti-Stokes phonon lines from a single Si nano-wire.

of the interatomic potential.

The extrapolated "zero" power spectrum on the other hand should give the confinement effects. However in this example where the nano-wires have thicknesses of 100 nm or more such confinement effects are probably not very significant. Nanowires with smaller thickness ($<$10 nm) should be used to study confinement effects in quasi-1D structures.

## 4.5 Surface vibrations

GaAs nano-rods (Fig.4.1a) grown by the Vapor Liquid Solid (VLS) method [18] in the (111) direction on GaAs(111) substrates in an oriented fashion were obtained from the University of Lecce [20]. They have diameters of approximately 60 nm and lengths in the micrometer range. The measurements were performed on the samples as they were grown. Single nano-rods were selected in the low

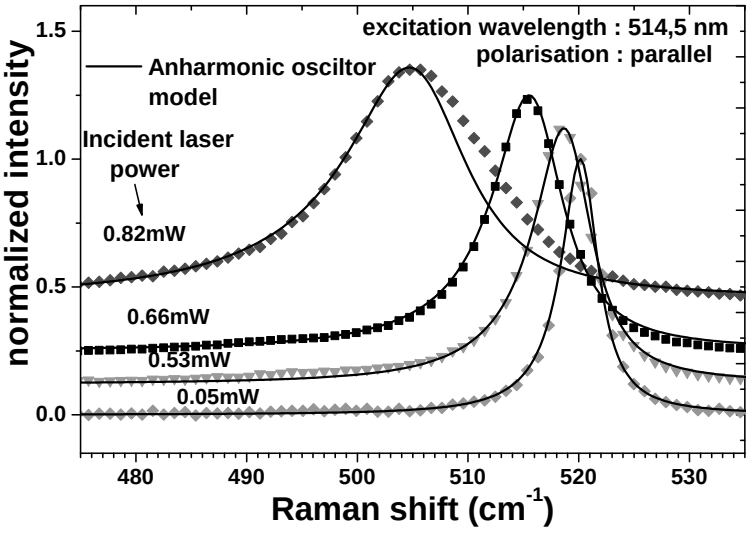


Figure 4.7: Excitation power dependence of Raman spectra from a single Si nano-wire. Redshift and asymmetric broadening appear at higher excitation power. For the lowest power the line is symmetric. A line splitting possibly occurs for the highest excitation power. The phonon spectra are fitted by numerically calculated anharmonic oscillator model line shapes (3.6.2).

nano-structure density area of the sample and positioned into the micro-focus by moving the sample on a nanometric stage. In order to distinguish the Raman signal of the nano-rods from the Raman scattering from the substrate (both nano-rods and the substrate are crystalline GaAs) the focal plane of the confocal microscope was placed $\sim 1\mu$m above the substrate surface.

The spectra of the GaAs nano-rods show a strong dependence on the applied laser power due to the heating of the rods by the laser beam (Fig.4.8 [21]).At comparably low laser power density (several mW per $\mu m^2$) the small volume of the nano-structures can already be heated easily up to several hundred K above room temperature. As a result, shifts of the phonon frequencies to lower values and a line shape broadening are observed similar to that observed for Si nano-wires. The anharmonicity of the lattice potential in GaAs

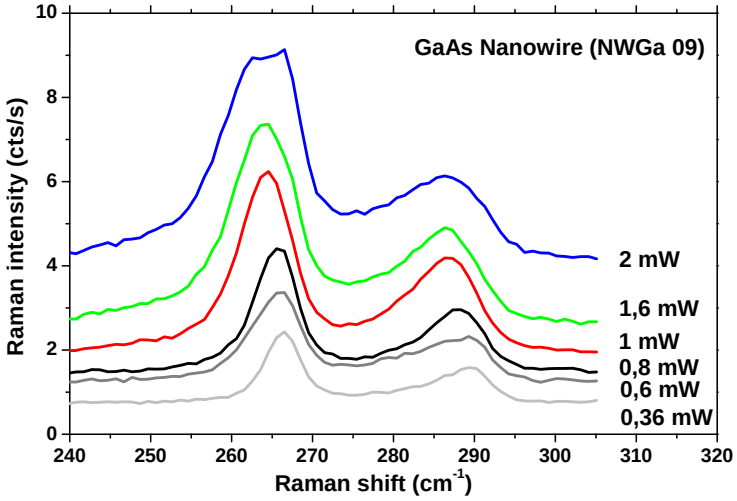


Figure 4.8: Excitation power dependence of Raman spectra from a single GaAs nano-rod. Redshift and asymmetric broadening occur for both the LO and TO phonon modes. For the highest excitation power a line splitting of the TO line is clearly visible.

[50, 85] is the cause for these modifications with laser power. With increasing exiting laser power increasing asymmetry of the LO and TO phonon lines is observed (see Fig.4.8. The fact that both LO and TO are asymmetrically broadened and additionally the TO line splits for high power can be interpreted in terms of inhomogeneous temperature distributions in the nano-rod.

As already mentioned above the influence of the heating should be avoided and only low excitation laser power can be used in case the dimensional effects are investigated. In the measurements shown in Fig.4.9 a laser power of 180 $\mu W$ from the 2.41 eV laser line was used after a series of measurements with lower and higher powers at an another GaAs nano-rod sample.

From the low power Raman spectra of the GaAs nano-rod sample in Fig.4.9 (two upper panels) it was found that the TO phonon frequency corresponds to that of the bulk. This is expected since the

diameter of the nano-rods (60 nm) is not sufficiently small to result in a quantum confinement of the phonon modes. But for the LO phonons a remarkable change in the appearance of the phonon line is clearly visible in the spectra. Several new modes appear in the

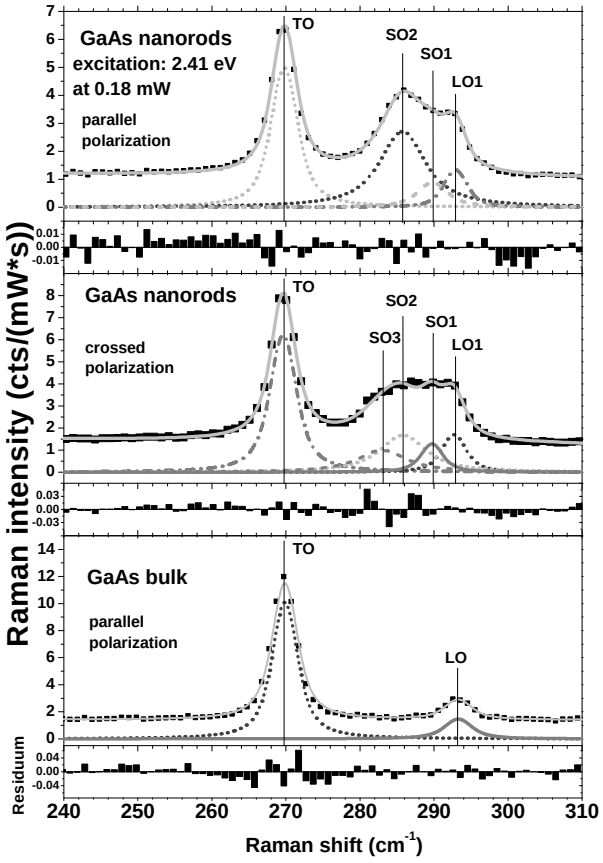


Figure 4.9: Raman spectra from a single free standing GaAs nano-rod (two upper panels) and GaAs bulk (lower panel). The three spectra are fitted by Voigt line shapes in order to verify quantitative frequency shifts. No significant frequency shifts of the LO and TO phonons from the nano-rods with respect to the bulk could be verified. In comparison to bulk spectra new lines appear in the nano-rod spectra in the gap between TO and LO phonons. The new phonon lines are sensitive to the polarization of the excitation laser light. This can be seen from the comparison of the upper and middle panel spectra.

TO-LO gap and dominate the LO region. A simple explanation for their appearance would be that the macroscopic LO phonon electrical field acts at longer distances (phonon wave length) and already "feels" the boundaries even in these rather large structures. In contrast, the TO phonons, arising from the short range crystal potential forces, would need smaller dimensions to experience confinement.

Another interpretation of the phonon modes of the III-V nano- structures appearing in the TO-LO gap was given by Gupta et al. [86] in the case of GaP nano-rods. According to this interpretation the surface modes of the GaP nano-rods (diameter 20nm and 50nm) dominate the spectra due to the large surface/volume ratio. The frequency of these surface modes is determined by the electric field on the surface [87].

A third explanation could arise from diameter variations of the nano-rods, especially periodic ones occurring through the growth process.

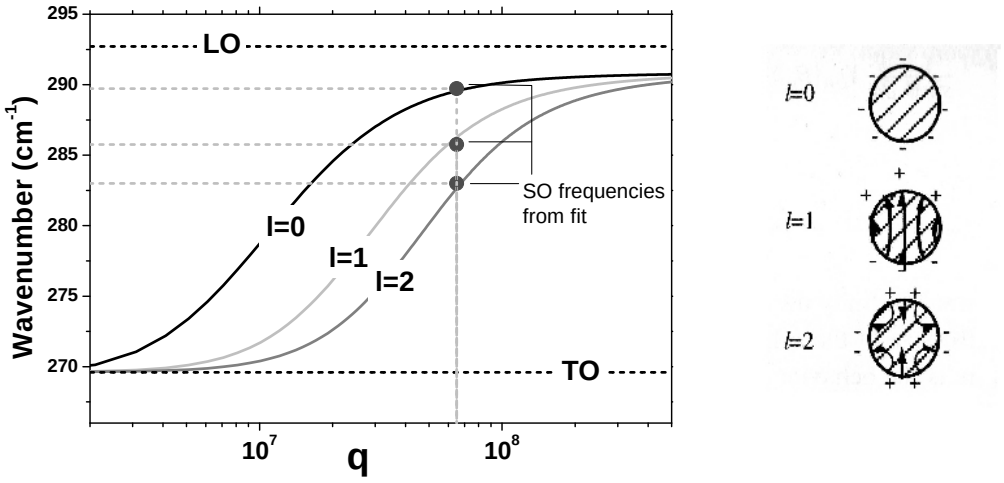


(a) (b)

Figure 4.10: On the left: surface modes (SO) dispersion of a 60 nm diameter GaAs cylinder in air, calculated by Eq.4.6. On the right: surface charge distribution on a dielectric sphere for different oscillation modes (l=0,1,2 in eq.4.6).

They could lead to zone folding effects for k-vectors along the axis of the nano-rod . The effect on the low dispersive TO phonon would be small but the LO phonons, having the stronger dispersion, could appear with different frequencies.

According to the continuum model the surface oscillation mode frequency on a circular cross section nano-rod in air (dielectric constant $\approx 1$) can be calculated by [87] with $x = kr$ (r- nano-rod radius, k-momentum)

$$\omega_{SO}^2 = \omega_{TO}^2 + \frac{\omega_p^2}{\epsilon_\infty + \epsilon f(x)} \tag{4.6}$$

$$\texttt{with} \quad f(x) = \frac{I_l(x)K_{l+1}(x)}{I_{l+1}(x)K_l(x)},$$

$$\texttt{and} \quad \omega_p = \sqrt{\epsilon_\infty \left(\omega_{LO}^2 - \omega_{TO}^2\right)}$$

where $\omega_{LO}^2 = 293 \quad cm^{-1}$ and $\omega_{TO} = 269 \quad cm^{-1}$ are the frequencies of the bulk longitudinal and transversal optical phonons respectively, $\epsilon_\infty$ is the high-frequency dielectric constant of the GaAs bulk. $\omega_p$ is the plasma frequency, screened by the dielectric, with $\epsilon_\infty$. $K_l(x)$ and $I_l(x)$ are modified Bessel functions. By setting $l = 0, 1, 2, 3...$, dispersions for modes with different charge distribution can be obtained. In Fig.4.10 (on the right) charge distributions for a dielectric sphere with different symmetries (corresponding to l=1,2,3) are shown. In a cylinder, however, the charge distribution is similar, but additional distributions (alternating) along the nano-rod axis are present.

The nano-rod diameter was measured by scanning electron microscopy and is in the range of 60 nm. Using this information the dispersion relation of the surface modes can be calculated (Fig.4.10). By comparing the SO frequencies from the fit in Fig.4.9 with dispersion relation for the SO modes, an assignment of the measured frequencies to the SO modes types is possible. According to this assignment the $SO_2$ mode at $285.5 \pm 0.2 cm^{-1}$ is due to a dipole like

charge distribution and the $SO_2$mode at $283.0 \pm 0.2cm^{-1}$ belongs to a quadrupole-like charge distribution. This explains the polarization dependence of the spectra in Fig.4.9: while in crossed polarization the quadrupole mode is more intense, the dipole mode is dominant with the parallel polarization.

From Fig.4.10 the estimation of the total momentum of the surface vibrations is possible. Similar momentum for the surface modes can be assumed because of the same geometry of the nano-structure. The periodicity obtained from the momentum is ca. $105 \mp 10nm$ which corresponds to half the circumference of the GaAs nano-rod.

## 4.6 Resonant Raman scattering in nano-structures

Due to the small volume of nano-structures, Raman scattering from such small quantities of matter suffers a drawback in giving only weak intensities. This is particulary disadvantageous in the case of strong background signals coming, for example, from the substrate. Thus resonant Raman scattering, which is able to greatly increase the Raman signal, is a useful technique in order to improve the signal-to-noise ratio of the spectra and to enable their quantitative analysis.

ZnO shows a strong resonance behavior as can be seen in Fig. 4.11(a) with the example of two Raman spectra of bulk ZnO taken with different laser lines. They are in general agreement with the data which have been published in the past [88, 89, 90, 91]. The spectrum with the 647.1 nm (= 1.95 eV) line of a Krypton laser is non-resonant with respect to the band gap of ZnO (3.3 eV) while the 406.7 nm (= 3.05 eV) line is near resonant. Enhanced scattering intensities with the latter excitation can clearly be seen in Fig. 4.11. Under such resonant conditions it should be possible to distinguish phonon spectra from nano-structures from the spectra of the substrate.

By using near resonant excitations (406.7 nm), Raman measurements

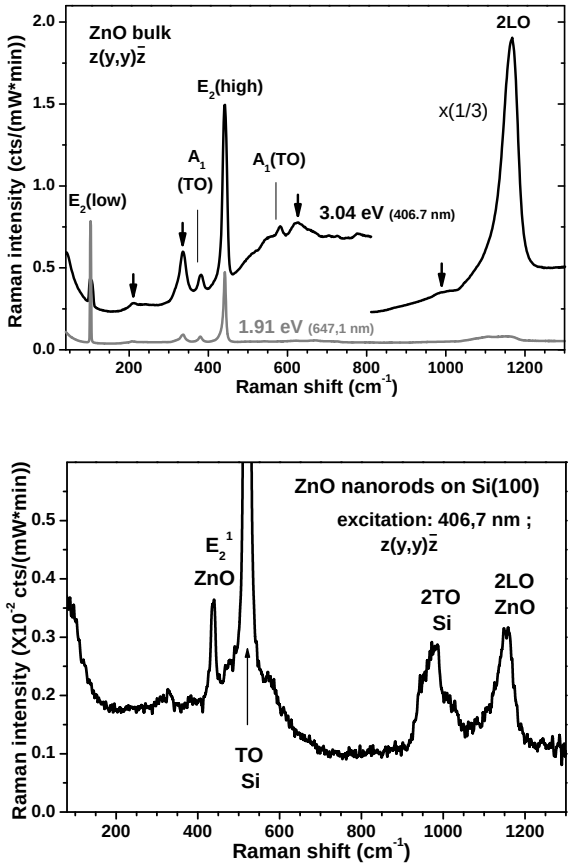


Figure 4.11: Raman spectra of ZnO: (a) bulk ZnO, for two different laser lines. With 647.1nm excitation a non-resonant Raman spectrum is obtained. The 406.7 nm spectrum is **near resonant** showing a larger scattering intensity and a number of second order phonon peaks, 2LO and lines indicated by arrows. The indexed capital letters refer to the irreducible representations of the point group $C_{6v}$ of wurtzite ZnO.; (b) ZnO nano-rods on a Si(100) substrate, luminescence background has been subtracted. Due to near resonance conditions enhanced $E_2^1$ and 2LO modes are observed.

of ZnO nano-rods (sample similar to Fig.2.3, but which are lower density) grown by CVD on Si(100) substrate were possible (Fig. 4.11 b). In spite of the low ZnO nano-rod density on the substrate surface (approx. 5 nano-rods per $\mu$m$^2$, each one approximately 40 nm thick

and 300 nm long) and hence, a small scattering volume, identification of ZnO vibrational modes ($E_2$, 2LO) is possible. No size-related frequency shifts, however, were detected within the accuracy of this measurement ($\approx 1\,cm^{-1}$). The size of the the ZnO nano-rods is probably still not small enough to generate observable phonon shifts as reported in the literature [92].

## 4.7 Nanometric and sub-nanometric structure

Recently developed growth methods enable synthesis of 0- and 1-dimensional nano-structures having internal structure, for example core shell structures or alternating heterostructures. The goal is the synthesis of heterojunctions in order to exploit their properties similar to the heterojunctions of bulk materials. In such structures material properties alternate on nanometric or even sub-nanometric scale. The use of ternary or quaternary materials often leads to non homogeneous composition distribution and hence spatial variation of properties. An example of a Raman spectrum of an internally inhomogeneous nano-structure is shown in Fig.4.12 where by means of micro-Raman spectroscopy the quantitative determination of the ternary composition of an ensemble of VPE grown AlGaAs nano-rods is demonstrated. The concentration of Al is revealed by the evaluation of the phonon line shifts in the GaAs-like and AlAs-like spectral ranges. The appearances of several phonon mode groups (marked with connected lines), every group belonging to a certain composition, suggest a non uniform distribution of the components. Since, due to the spatial resolution limit of conventional optics, several nano-structures are supposed to be within the excitation area, it is impossible to conclude if either nano-structures with different compositions are observed or each single nano-structure possesses an inhomogeneous material distribution.

Until now Raman spectroscopy from nano-structures consisting of

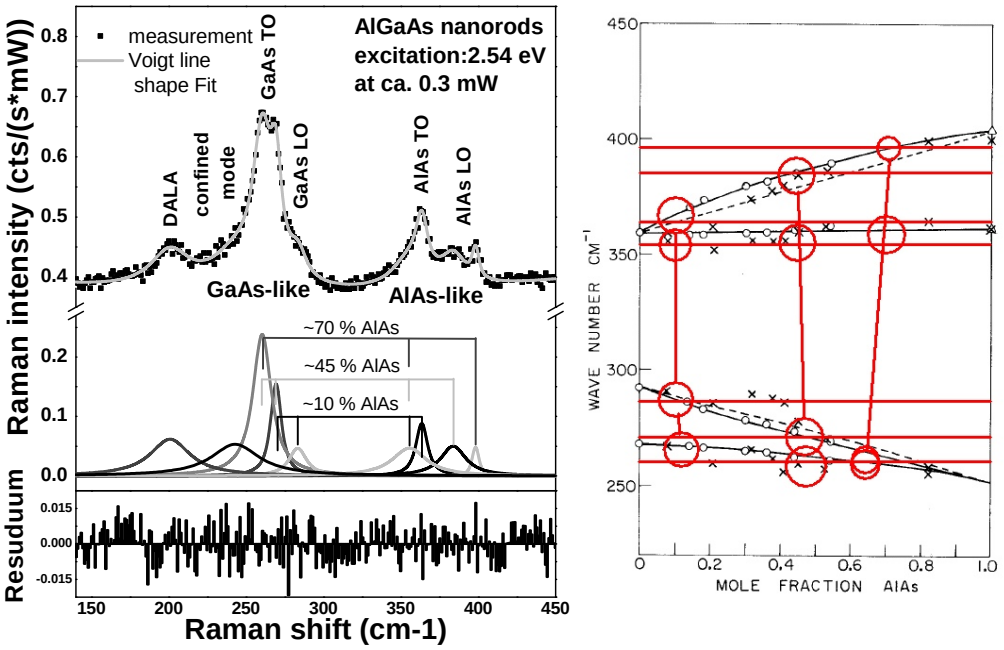


(a) (b)

Figure 4.12: Quantitative determination of the ternary composition of AlGaAs nano-wirws. a) Raman spectra of an ensemble of AlGaAs nanorods and its fit by Voight line shapes. The ternary composition of the nano-structures is revealed by the evaluation of the phonon frequencies in the GaAs and AlAs like wavenumber range. The presence of three different phonon line groups in the spectra (indicated by connected lines in the middle panel) suggest a non homogeneous distribution of the ternary alloy components. b) Dispersion analysis of the optical phonon frequencies in the AlAs and GaAs like frequency range versus the AlAs molar content in the GaAlAs bulk. While empty circles and crosses indicate the experimental results (taken from [93] and references from it), the solid and dashed lines represent the calculation by modified Chang-Mitra model [94] from [93].The red lines indicate the frequencies extracted from a) and the red circles stand for the probable assignment of the frequencies to the dispersion relation.

materials with known composition and structure were presented. This structures can be still represented as size-reduced bulk materials. Already known bulk parameters (phonon dispersion) are the

| Measured spectra ($cm^{-1}$) | Si sheet calc. ($cm^{-1}$) | Type of vibration |
|---|---|---|
| 70,76,84,91 | – | |
| 133, 270 | – | |
| 327 | 381 | transversal vibration with participation of H |
| | 481 | H symmetric vibration parallel to plane |
| 519 | 493 | longitudinal mode with participation of H |
| 717 | 689 | H asymmetric vibration parallel to plane |
| 805 | | possible $Si - H_2$ scissor bending |
| | 2073,2088 | Si-H stretching |

Table 1. Measured and calculated vibrational frequencies of Si nano-structures. First column contains data from Fig.4.13. Data in the second column are taken from calculations of vibrational spectra for Si single sheet saturated on both sides by hydrogen atoms.

basis for the interpretation of the spectra. There is, however, a large amount of nano-structure types with unknown vibrational properties. An example of those are silicon nanotubes whose structure significantly differs from silicon bulk.

There is a large interest in one-dimensional silicon structures as possible elements of nano-electronic devices. Efficient methods of silicon nano-wire growth are already present in the literature. However, freestanding nano-wires have diameters ranging from few to hundreds of nanometers. Further reduction in dimension requires new concepts. Stable single walled silicon nano-structures with diameters in the nanometer and sub-nanometer range similar to carbon single walled tubes were suggested by theoretical calculations [95][96]. Many different structures models for Si nanotubes were suggested. Some of them differ significantly from each other as proposed structural models involved either sp2 or sp3, or sp2-sp3 mixed hybridizations [95].

Recently growth of Si nanotubes by molecular beam epitaxy (MBE) was reported, however these tubes have a large diameter ($> 50$ nm), large wall thickness of 4-6 nm [97], and are embedded in $SiO_x$ lay-

ers. Synthesization of non oxidized silicon nanotube by the gas phase condensation method without SiO sheet was also reported [98]. The latter is especially suited for comparisons with already ex-

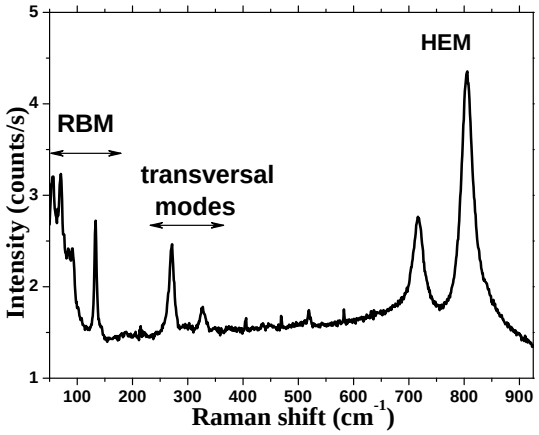


Figure 4.13: Presumable Raman spectra of of Si nanotubes. High energy modes (HEM) at ca.700 and 800 $cm^{-1}$ belong probably to the H-Si-H scissor bending vibrations. The lines in the central region at 327 and 519 $cm^{-1}$ are probably transversal and longitudinal Si plane vibrations respectively while lower frequency vibrations could be the tubular radial breathing modes (RBM).

isting theoretical models, because of their oxygen free composition. STM imaging of these nanotubes [98] indicate an atomic arrangement compatible with a puckered structure and different chiralities. However, there are still open questions about the structure apart from the general question searching the atomic arrangement. For example, whether the Si bonds saturated by hydrogen or not, and what is the type of sp hybridization? Questions about structure may possibly be answered by vibrational spectra combined with theoretical calculations.

Raman spectroscopy on samples investigated in Ref.[98] was performed in our laboratory by using a 514.5 nm laser line at low power (<1 mW) in order not to damage the sample by heating. One possible Si nanotube spectra is shown in Fig.4.13. The spectra show two intensive lines at ca. 700 and 800 cm$^{-1}$ which can not belong to Si-Si vibrations because of their high frequencies. $Si - H_2$ scissor bending vibration has a similar frequency (ca. 950 cm$^{-1}$), however. A saturation of Si bonds seems thus reasonable in this structure. Other vibrational frequencies from this spectra are summarized in Table

4.7.

The dynamics of nanotubes are comparable to the behavior of plane sheets because a nanotube can be imagined as a rolled up plane (similar to carbon nanotubes). Theoretical results for a Si sheet can be used to calculate the main vibrational modes of the nanotubes as well. Calculations were performed by an ab-initio method within the density functional theory [99]. Relaxation of the structure (bond saturation by H atoms) reveals a buckled three fold symmetry (hexagonal) structure with $sp^3$ hybridization. Calculated vibrational modes are compared to the spectra in Tab.4.7. The Si-H bending mode at 689 cm$^{-1}$ correspond probably to the 717 cm$^{-1}$ mode from the spectra. The Si sheet vibrations at 481,493 cm$^{-1}$ and 381 cm$^{-1}$ could be associated with the experimental value 519 cm$^{-1}$ and 327 cm$^{-1}$. The experimentally obtained modes below 300 cm$^{-1}$ could be the result of the tubular geometry of the structure (similar to radial breathing modes in carbon nanotubes).

Comparison of the measurements to the calculations is not yet satisfying. Changing the theoretical model to a Si plane sheet saturated by hydrogens on only one side could be sufficient to reproduce the mode at ca. 800 cm$^{-1}$ which could correspond to the $SiH_2$ scissor. It would also slightly change the Si-Si frequencies. The possible vibrations of the tubular structure could be only reproduced modelling a tubular structure. Moreover, measurements in the range of 2100 cm$^{-1}$ (Si-H stretching modes) are necessary in order to obtain conclusive results on the existence of hydrogen saturation.

## 4.8 Conclusions for micro Raman results

Several examples of low dimensional structures were discussed. Phonon parameters could be extracted by Raman scattering. From the experimental side one can thus be quite optimistic about the role of Raman scattering for low-dimensional physics. The spatial res-

olution given by optical microscope techniques ($\approx 1$ $\mu$m) limits its exploitation to the investigation of nano-structure ensembles or at best entire structure since the properties within the excited spot are averaged and no specific information on nano-scale can be extracted. Information on individual internal structure (e.g. hetero-junctions) of the nano-structures is not accessible at micrometric spatial resolution. What needs to be technologically improved are thus the high spatial resolution techniques. Theoretically the situation is also rather unsatisfying at the moment. Calculations within the quantum mechanical models for interpretation of the observed (or not observed) frequency shifts with respect to materials and geometry are urgently needed.

# Chapter 5

# The optical Nearfield

The resolving power of optical instruments in the far field (sample-observer distance $>> \lambda$) is in the order of the wavelength (Equ. 6.6):

$$\Delta r = 0.6098 \frac{\lambda}{NA}, \tag{5.1}$$

whit $\lambda$ the light wavelength and $NA$ the nummerical aperture of the optics.

Since the diffraction limit does not allow us to focus light to dimensions smaller than roughly half a wavelength, it is not possible to interact selectively with nano-scale features by means of diffractive optics based on a lens microscope. In recent years several new approaches have been put forth to 'shrink' the diffraction limit (confocal microscopy) or to even overcome it (near-field microscopy). The Scanning Nearfield Optical Microscope (SNOM) utilizing glass fibre tips with sub-wavelength apertures was developed to overcome the diffraction limit. Unfortunately it suffers a severe loss of intensity restricting it to be utilized with strong intensity optical processes (e.g. photoluminescence). Raman scattering, being a weak intensity process, depends on techniques which avoid losses in intensity. Aperture less SNOM (a-SNOM) which exploits the tip-enhancement effect, can be utilized to perform Raman spectroscopy and imaging with a spatial resolution of less than 20nm. To date,

this is the highest optical resolution of a spectroscopic optical measurement.

## 5.1 Diffraction of plane waves from a slit

In conventional imaging and microscopy the light collecting optics is always in the far field (distance $\gg \lambda$, the light wave length) of the investigated object. The optical information on the sub-wavelength structure of the object disappears in between. We demonstrate this by showing simulated diffraction patterns (Fig.5.1) of slits illuminated by a plane wave for different distances from the slits. The exact calculation of the light transmission through a small aperture requires a self consistent solution of the Maxwell equations [100, 101]. But in order to obtain the qualitative behaviour of the diffraction the problem can also be treated by means of a simple scalar theory. The simulated diffraction patterns in Fig.5.1 were obtained according to Huygens' principles, by assuming that every point in the space between the slit borders is the origin of a spherical wave and summing up the scalar field intensity of these waves at the desired coordinates:

$$I = E^2 = \int^T \int^A \frac{\exp^{-i(\mathbf{kr}-\omega t)}}{\mathbf{r}} \mathsf{d}a\mathsf{d}t \qquad (5.2)$$

where A is the area emitting the spherical waves (composed of one or two finite size slits), $a$ is the position within the slits, $T >> (1/\omega)$ is the integration time, k is the wave vector, $\omega$ the frequency of the light and **r** the distance from the origin of a single spherical wave.

The calculated diffraction pattern in Fig.5.1 shows on the right hand side ($d = 100\lambda$, far field) the well known Fraunhofer diffraction pattern. For wide slits (w = $3\lambda$, Fig.5.1a) the far field diffraction is similar to the well known Airy-function pattern which gives the resolution of Eq. 6.6. For a smaller slit (in Fig.5.1b), with slit width d= $\lambda/10$), nearly uniform scattering into the right half space (similar to a simple spherical wave) is observed.

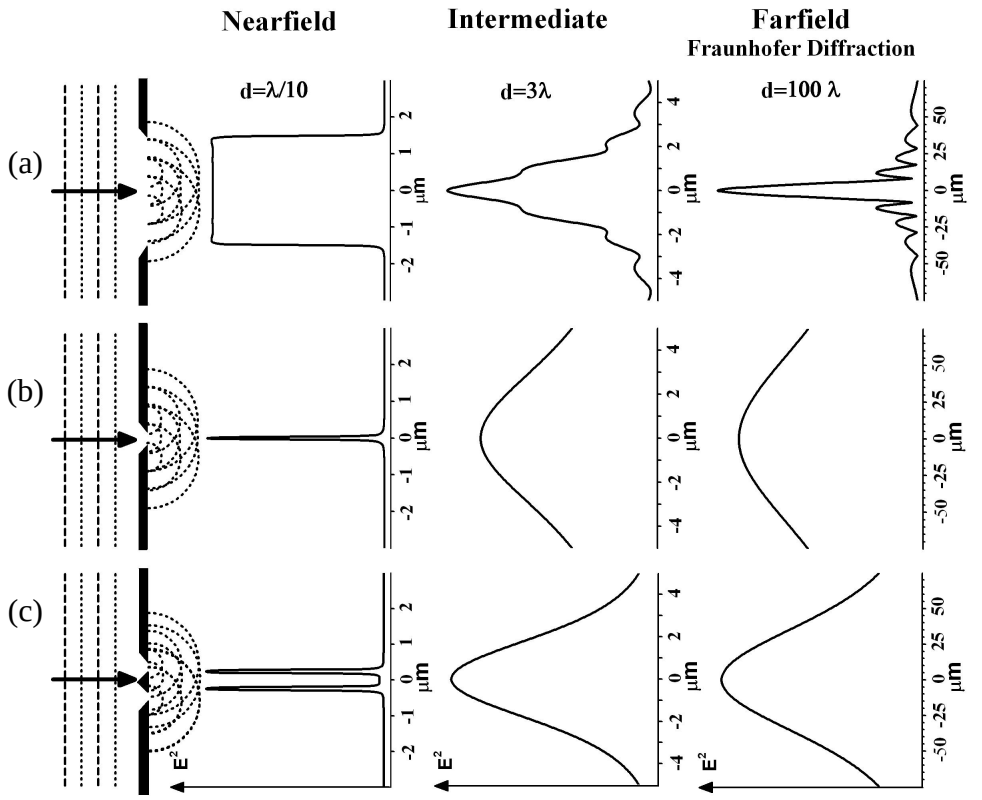


Figure 5.1: Simulated intensity patterns from transmission of narrow slits (infinite length) calculated by summing the secondary spherical waves originating in the slits (eq.5.2). The infinite slits are illuminated by a plane wave at $\lambda = 500nm$ from the left. The largest single slit (on top) has the size of three times the wavelength, the narrow slit width (in the middle part) is ($\lambda/10$). The double slit (lower part) is consistent out of two $\lambda/10$ slits separated by $\lambda/2$ spacer. On the right the far field intensity distribution in the half space is shown. In the left graph the near field intensity is calculated at 10 nm distance from the slit plane. In case of the large slit the well known Fraunhofer diffraction pattern appears in the far field. The intensity distribution in the far field for the small slits is nearly uniform and similar to a single spherical wave. In the near field the intensity pattern is not generated by diffraction like in the far field. In the case of the double slit a well distinguishable double structure in the light intensity pattern indicates the sub-wavelength size and distance of the slits. The two structures are not distinguishable in the far field .

The phase difference of the spherical waves originating at the slit is not sufficient to create a diffraction pattern with several maxima. Even in the case of two narrow $\lambda/10$ slits separated by a $\lambda/2$ spacer, shown in the lower part of Fig.5.1, the phase difference (caused by the distance between the slits) is not sufficient to make the two small slits distinguishable in the far field.

However, in the proximity of the slit plane within a distance of a wavelength fraction ($\lambda/10$) to the slits (Near Field) the diffraction pattern of the single slit (b) and the double slit (c) are clearly distinguishable and display the structure of the object. Thus sub-wavelength structures can be resolved. This sub-wavelength structure information with spatial frequencies larger than $k > \frac{1}{\lambda}$ is carried by the non-propagating near field which does not contribute to the far field pattern [102].

## 5.2 Optical Near Field Microscope

Aperture scanning near-field microscopy is a technique that allows for arbitrarily small details to be resolved. It works by scanning a small aperture in the proximity of the object (Fig.5.2). The distance between the aperture and the object plane is in the order of nanometers and is critical for the resolution. Light can only pass through the aperture, and so this size also determines the resolution of the system. This technique is typically implemented by tapering an optical fiber to a narrow point and coating all but the tip with metal. By this method, images with a resolution far beyond what is possible with traditional microscopy can be recorded.

However, the amount of light that can be transmitted by a small aperture poses a limit on how small it can be made before nothing gets through. To a degree this is acceptable, as more optical power can be generated, but the cutoff is so severe that the aperture cannot be made smaller. When the aperture is 100 nm, the cutoff is down four

orders of magnitude, and when it reaches 50 nm, only one part in $10^8$ makes it through. Furthermore, the input power cannot be increased arbitrarily because $1/3$ of the power is absorbed in the coating. Increasing the input power above approximately 10 mW will destroy the coating. This severely limits the signal-to-noise ratio of small apertures, and is the reason our group uses another approach.

Instead of using a small aperture, we use a metal tip to provide a local excitation. If a sharp metal tip is placed in the focus of a laser beam, an effect called local field enhancement will cause the electric field to become much stronger. This enhancement is localized to the tip, which should have ideally a typical diameter of 10 nm. As this tip is scanned over the surface, an image can be formed with a resolution as fine as the tip [9].

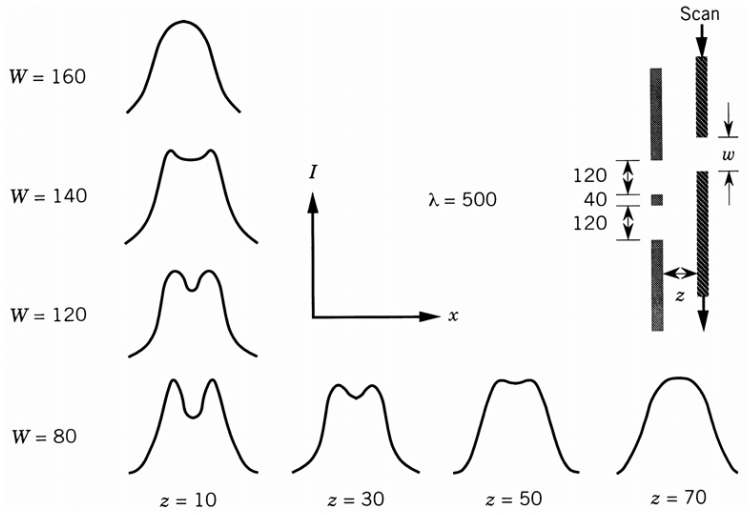


Figure 5.2: Simulated aperture near field optical microscope scan lines. The resolution depends on the aperture size and the distance from aperture to the sample plain. The smaller the aperture and the distance the higher is the simulated resolution.

## 5.3 Tip Field Enhancement

.

The field enhancement is needed to generate appropriate optical signals, which results from the strong optical interactions between the tip apex and the sample. It is a complicated function of many parameters, such as the geometry of the tip, its surface state and material parameters, etc. Anyway, enhancing the electric field of a body, in general, and of the tip in particular is a nontrivial problem. It is especially important for the development of tip-enhanced Raman spectroscopy because the (usually very weak) Raman signal rises as the fourth power of the field [102]. A problem arises how to choose optimal conditions for achieving maximal enhancement of the strongly localized electric near field. These include choosing enhancement mechanism and the tip-surface geometry, as well as the tip material/shape combination.

Beside of a valid model of the tip/sample configuration a computational (numerical) algorithm is needed in order to handle all these parameters under realistic conditions. Metallic particles, tips included, respond much more to the magnetic fields in comparison to dielectric glass fibre tips. Hence a treatment of electrical fields only is not sufficient. A complete set of Maxwell equation needs to be solved.

In last years Finite-difference Time-domain (FDTD) became a widely used method for field enhancement calculations [103, 104, 105, 106, 107]. This is a numerical algorithm which solves a discrete formulation of Maxwell´s equations to calculate field values throughout a defined problem space after each of a series of time steps. Charge distributions may be calculated from the divergence of the electric field. For the purpose of defining the material parameters to describe a particular system, the problem space is discretized into cells. The cells are not larger than a tenth of the light wavelength in order to

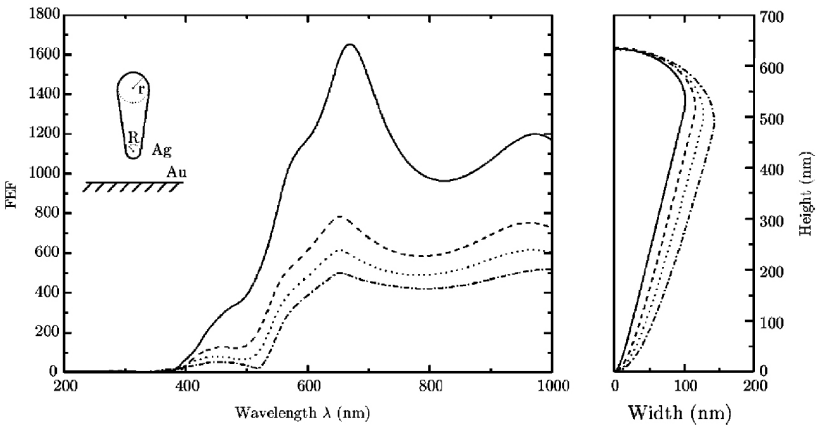


Figure 5.3: Dependence of the Field enhancement spectra on the apex radius (from [106]). R=10nm (full line), R=30nm (dotted), R=50nm (dashed), R=80nm(dash-dotted line).

accurately sample the field distributions. Each cell is is characterized by its local electromagnetic properties and by the electric and magnetic field vectors. The total simulated volume for the calculations is limited only by the computational effort and is at the moment around a cubic micrometer.

In Fig.5.3 calculations of the field enhancement factor of a silver tip in the proximity to a gold substrate are shown. The tip enhancement depends strongly on the size of the tip apex. The smaller the tip the higher are the enhancement factors.

The enhancement mechanism is related to the plasmon frequency in the tip material. Collective electron oscillations (plasmons) excited by the laser generate a local oscillating field. Because the plasmon eigenfrequencies depend on the material properties, the choice of the tip material is important in order to achieve optimum enhancement. This, however, is important for energies near the plasma frequency (Ag 3.9eV, Au 1.9eV); at lower frequencies the antenna effect is more important. The amplification varies according to the shape of the tip (apex diameter, conical angle). Regarding the apex diameter there is a general consensus in the literature that the smaller tips provide a higher field enhancement. Concerning the conical angle

of the tip, however, an agreement has not yet been reached.

Polarization is an important issue for the enhancement optimization. As can be seen in Fig.5.4 the polarization orientation parallel to the tip axes generates much stronger field enhancements. This fact should be considered for the selection of the scattering geometries. The most simple way to achieve excitation of the tip by parallel polarization is through illumination from the side. In this case the polarization of the incoming laser beam can be easily adjusted along the orientation of the tip. Frontal illumination (from the tip apex side) is also possible without losses in efficiency. For this type of tip illumination geometry a so-called "z-polarization" is needed (polarization parallel to the propagation aches, generated by focusing of radial polarized laser beam) [108, 109]. Radial polarization of the incoming laser beam is necessary before the focusing of the laser light on the tip.

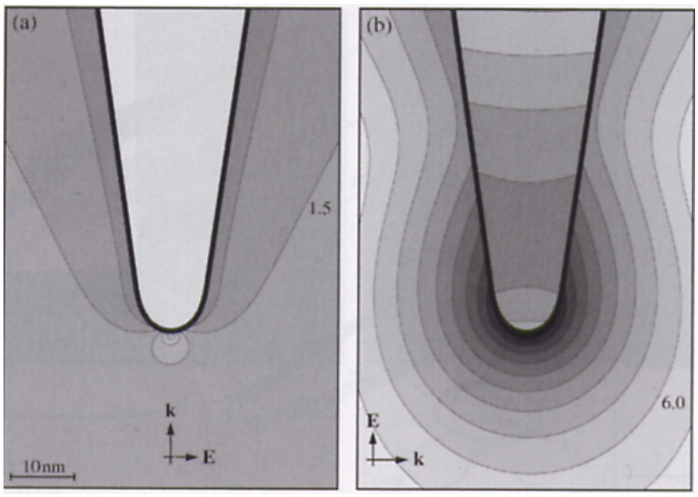


Figure 5.4: Influence of the incident light polarization on the Field enhancement of a tip. On the left: illumination of the tip by polarization perpendicular to the tip. On the right: parallel polarization is utilized. From [102]. The enhancement near to the tip apex is approx $10^3$ (the intensity ratio between the sequent isolines is 2).

# Chapter 6

# Development of nanometric resolution optical equipment

From the previous discussions it is clear that experimental realization of optical near-field Raman scattering with coated optical fibers is difficult. Nevertheless it has already been tried since the beginning of the nineties [8], but due to intensity problems fiber applications were limited to samples with large Raman cross sections [7, 110]. On the other hand, apertureless techniques based on plasmon related resonant field enhancement, occurring for some metals in the visible spectral range, give a promising outlook for overcomming the intensity problem that is especially severe in Raman spectroscopy.

This plasmon resonance enhancement has been first observed in SERS (Surface Enhanced Raman Scattering) [111, 112] and exploited for very sensitive molecular identification [11, 13, 113]. Recent progress in computational theory of plasmonic properties of noble metal nano-particles [114] helps to optimize the metal tips with respect to their signal enhancement and the confinement of the near-field. Indeed, very recently apertureless techniques have been combined with a near field Raman scattering set-up for the first time [115, 116]. This concept is also referred to as TERS (Tip Enhanced Raman Spectroscopy) and its successful operation including the tip enhancement effect was shown for carbon nano-tubes [115]. Due

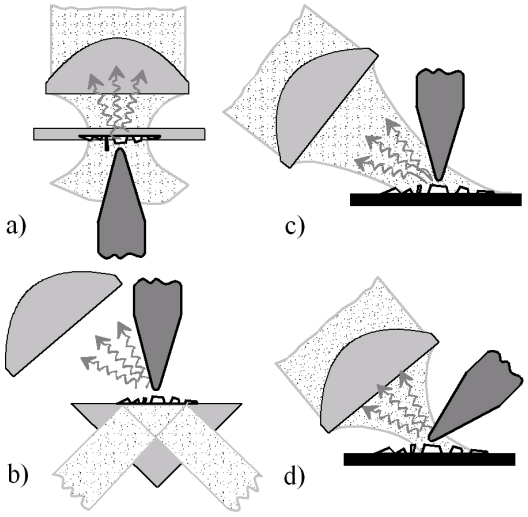


Figure 6.1: Nano-Raman configurations: a) transmission mode with high NA microscope objective, b) optical tunnelling mode, c) reflection mode, d) optimized reflection mode.

to the higher numerical aperture of this configuration those attempts are realized in the transmission mode while only few reflection mode TERS set-ups were exploited [13, 117].

Tip preparation is crucial for TERS measurements, because the radius, shape and material of the tip determine the enhancement factor and the spatial resolution.

## 6.1 Tip - sample - collection optics configuration

In Fig. 6.1 we show possible tip-lens-sample configurations for Raman scattering. A major advantage of the transmission mode (Fig. 6.1a) is that high numerical apertures are easily achieved using microscope objectives with short working distances and immersion. Thus the light can be efficiently focused and collected. The main disadvantage is that it is limited to samples deposited on transparent substrates.

In the mode represented in (Fig. 6.1b), the illumination is provided

by attenuated total reflection of a laser beam within a prism. Hence, in this configuration the tip and the sample are illuminated by the evanescent field which is generated at the interface while the illumination by the far field radiation is reflected into the prism. This configuration has a favorable signal-to-noise ratio as the tip is enhancing only the near-field, whereas in other configurations in Fig. 6.1 the far field is detected simultaneously with the near field. However, the optical properties of the prism may limit the spectral range of laser excitations or generate additional luminescence background. In analogy to the STM this configuration is usually called optical tunnelling mode.

A reflection mode is needed in order to explore samples on non-transparent substrates (Fig. 6.1c). In this geometry the tip (including distance control) and the optical set-up illuminating the tip and collecting the scattered light have to be arranged on the same side of the sample. As a consequence only long distance microscope objectives can be used and the numerical aperture available in this configuration is considerably decreased.

The reflection mode can be optimized with respect to the achieved field enhancement because it depends strongly on the illumination geometry [118]. The strongest field enhancement below the tip apex is observed if the polarization of the incident field is polarized along the axis of the tip. Furthermore, in theoretical models the tip is in general described by one or several dipoles. Considering their emission, a 90°-configuration is likewise favorable to efficiently collect the enhanced light (Fig. 6.1d).

## 6.2 Experimental set-up overview

We discuss the experimental configuration with the example of the set-up used at Roma "Tor Vergata" (Fig.6.2). Its different configurations allow for measurements on different spatial resolution scales:

macro-, micro- and nano-Raman spectroscopy. Common to all resolution scales is the laser illumination and the spectroscopic unit. By directing the laser light into different, parallel existing optical arrangements, the different spatial resolutions can be chosen.

The illumination source common for all set-ups is an argon-ion laser with a very low beam divergence (0.5 mrad) emitting mainly a $TEM_{00}$ mode. The mode purity is further enhanced by expanding the beam and by applying spatial filtering.

The spectroscopic tool common to all three resolution configurations is a triple monochromator that can be operated in a single line scanning mode (added dispersion) and in a multichannel mode as a spectrograph. The scanning mode provides a higher contrast and resolution when working with a low dark count photomultiplier. In the multichannel mode the first two monochromators operate in a subtractive mode, selecting the desired spectral region, to be analyzed by the spectrograph equipped with low noise, liquid-nitrogen cooled CCD (charge coupled detector).

The macro-Raman configuration is the standard Raman set-up and is mainly used when the experiment needs long working distances. It allows only the use of small numerical apertures (NA = 0.1-0.2) as is often the case with in-situ measurements in ultrahigh vacuum chambers, cryostats or gas cells. The resolution is thus low around $10 - 100\mu m$. The micro-Raman set-up is based on a confocal microscope design containing an objective with a very large numerical aperture (NA = 0.95) and a pinhole in the intermediate focal plane. The spatial resolution of this microscope is below 1 $\mu$m. In nano-Raman, where the optical near field is exploited, resolutions below 100 nm are achieved. Independent of the desired resolution, it turned out to be extremely important in all measurements on nanostructures, to have nano-positioning capabilities (nanometric stages) for the sample, in order to be able to increase the optical signal.

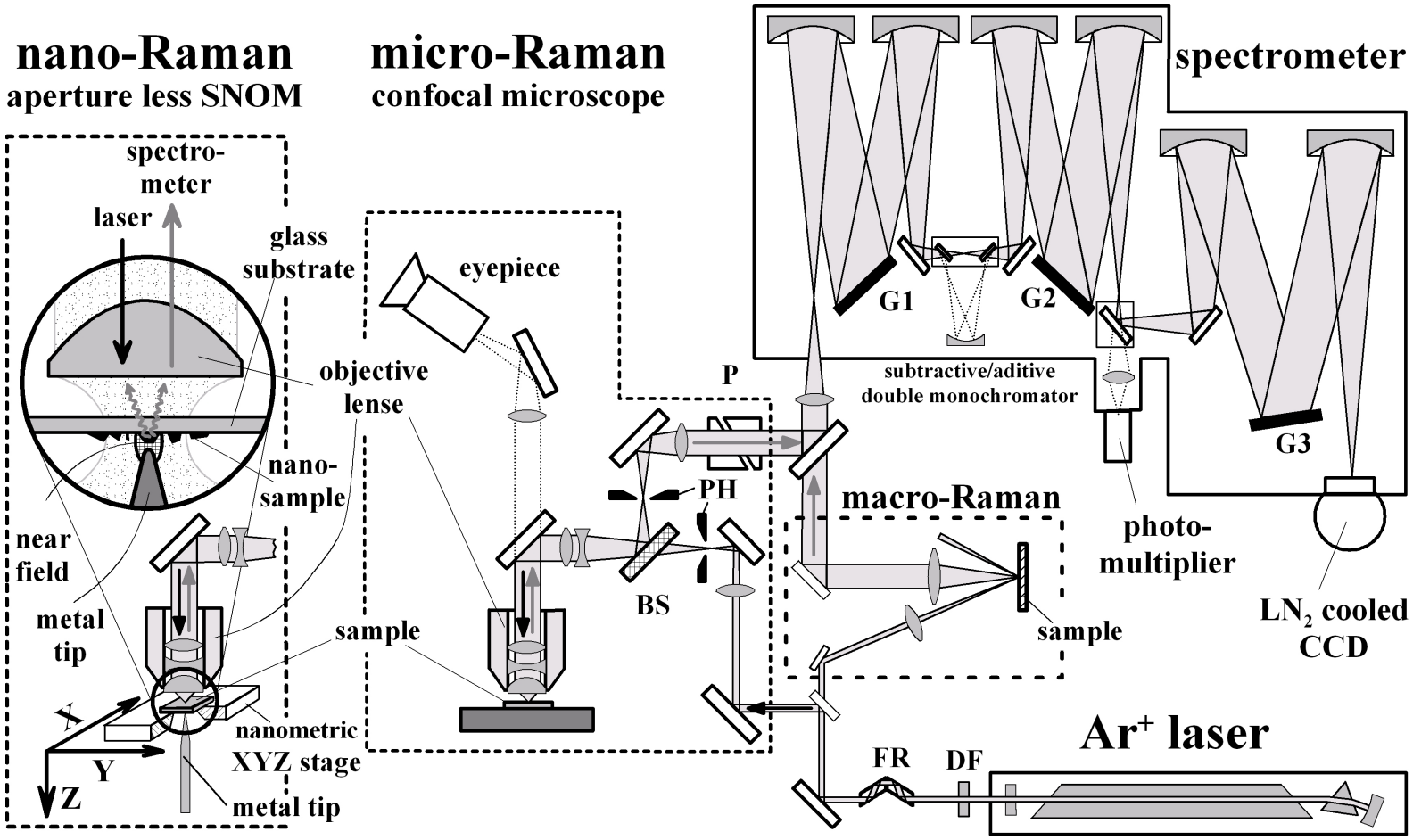


Figure 6.2: Raman setup with macro-, micro and nano-optics before the monochromator. **BS**-beam splitter; **FR**-Fresnel rombs; **PH**-pin holes; **P**-poliriser prism; **DF**-dielectric laser line filter; **G1,G2G3**-holographic gratings.

## 6.3 Vibrational isolation

Because SPM techniques are used in combination with the optical set up, an appropriate vibrational isolation of the set-up is needed. While a stiff connection between the scanned sample and the nanometric tip is necessary in order to prevent high frequency vibrations between the tip and the sample, the isolation of the whole set-up should be realized by low pass frequency mechanical filters which can be assembled by the low spring constant spring (e.g. elastomers or compressed air) and some energy dissipation elements (e.g. internal friction in elastomers or turbulent gas flow). In this section we discuss the vibrational isolation of the set-up from the external vibrational noise sources.

In the simplest case a suspension of the set-up on soft elastic rope is possible. The large mass of our set-up configuration including many voluminous and massive components like triple Raman monochromator, large frame laser sources and possibly a vacuum chamber (6.2) exclude this possibility. Instead an optical table with passive and active vibrational damping elements is utilized. The passive damping is consisting of compressed air suspension with low resonant frequency ( 2 Hz) and laminar air flow valves as dissipative damping elements. The active damping is realized by piezo driven actuators compensating the higher frequency vibrations (100 Hz - 1 kHz). The table body provides the necessary stiffness in order to avoid the vibrational eigen modes of the structure.

In contrast to many nanometric resolution near field optical measurement set-ups using a single laser line for excitation (usually HeNe laser 632.8 nm wavelength or 488 nm by small frame $Ar^+$ ion gas laser), we intend to exploit a wide range of laser frequencies from near UV to red which are available with the large frame ion gas lasers and the common HeNe laser sources. While HeNe lasers (because of their simplicity) can be mounted directly on the main experimental set-up structure, the large frame ion gas laser would

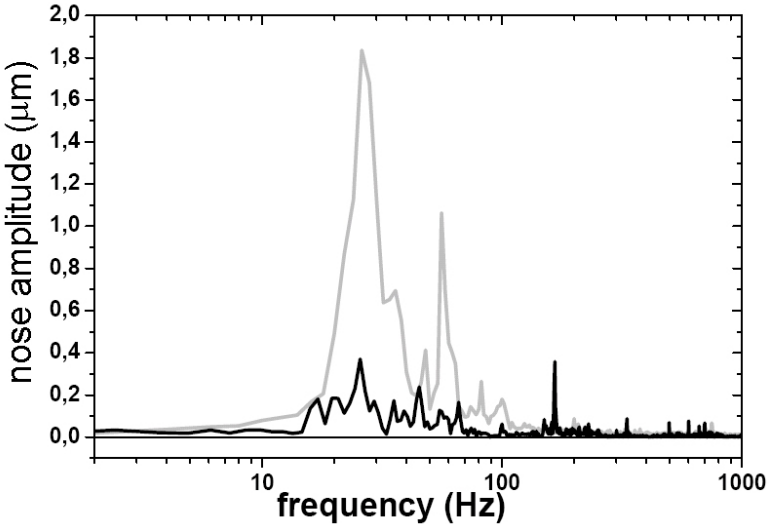


Figure 6.3: Comparison of vibrational spectra amplitudes with (black line) an without (grey line) additional laser suspension. A significant improvement is achieved by using additional suspension.


Figure 6.4: Photograph of the nano-Raman the set-up.

introduce an additional source of mechanical vibrations if mounted directly on the structure due to the water cooling circuit. Additional

vibrational isolation for the lasers is needed in order to damp the vibrations caused by the cooling water circuit.

## 6.4 Tip sample distance control

In near field spectroscopy a tip (either a glass fibre tip in case of aperture SNOM or a metal tip for apertureless SNOM) is held in the proximity of the sample. To obtain a nearfield signal the distances between the tip and the sample surface should be of the order of a small fraction of the light wave length. The near field contribution to the overall optical intensity in the nearfield experiment decreases rapidly with the increasing distance. The enhancement of the Raman signal decays on the length scale of 10 nm [107]. Sample tip distances in the nanometric range is therefore preferable. This is not a trivial problem. Obviously the distance should be kept constant in order to avoid the unwanted signal intensity modulations. A specific problem for tip assisted spectroscopy is the possible heating of the tip by the excitation laser. The thermally induced expansion of the tip could cause distance variations. It was found that for moderate illumination laser light power ($\approx$1mW) the temperature increase of the top remains in the margin of a few degrees K [119]. At least for set-ups using continuous laser sources, in contrast to pulsed lasers, this problem is thus not significant. Several distance control techniques are feasible for the near field technique. Although the distance regulation using the optical signal was shown to be usable, the low signal level and consequently low signal-to-noise ratio (SNR) avoid its practical application for the Raman spectroscopy. SPM methods like STM, AFM and their variations have proved to be reliable solutions for this kind of problem. In Fig.6.5 a scheme of an SPM electronic set-up is shown.

STM seems to be simple to implement in the use of the experiment because of conductive metal tips, but this is only valid for conductive

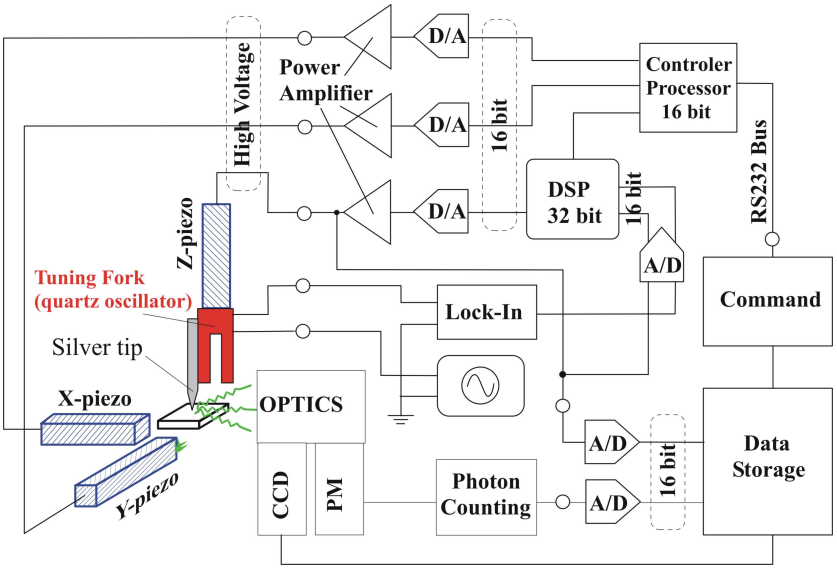


Figure 6.5: An example of SPM electronics for near field spectroscopy.

samples. Moreover the contact between the nanostructures and the substrate is not always conductive. This leads often to destruction of the sample and the tip. In contrast AFM has several advantages. No conduction is necessary for AFM and a larger distance margin for distance control for the AFM (Fig. 6.6) is available.

For distance control the use of piezoelectric quartz oscillators with attached tips [120] can be adopted from the glass fiber SNOM. The tuning fork fulfills the role of the cantilever. It vibrates at its mechanical resonance frequency. Sear force detection is used, i.e. the tip oscillates parallel to the sample surface. The advantage is that the tip is always in the proximity of the sample in contrast to non-contact AFM where tips vibrate perpendicular to the surface (with rather large amplitudes up to 40 nm). Another advantages of quartz cantilevers are a high thermal stability and low internal energy dissipation (higher Q factor).

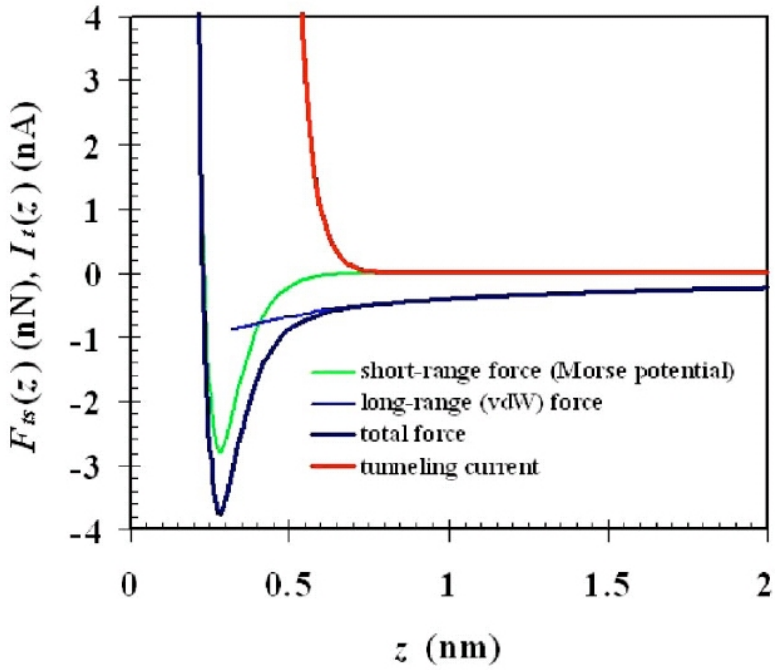


Figure 6.6: Typical sample probe distance dependency of the STM current and the force between the SPM tip and the sample. Exponential behavior of the STM current result in narrow practical margins for the distance control. The weak interaction (attractive) force allows probe sample distances control (several nm) in a wide range (>10nm).

### 6.4.1 Frequency modulated AFM

In amplitude modulated AFM the damped amplitude is detected and regulated to the desired level by regulating the distance of the oscillating tip from the sample surface increasing and decreasing the damping and as a consequence changing the resonance vibrational amplitude. Usually the oscillator is driven at a constant frequency. The transient oscillation from one amplitude level to the other is very slow (in order of 100 ms [121]) in case of high Q oscillators ("Quality" factor: $f/\Delta f$) resulting in a scanning time of several hours for only one AFM image. The use of low Q oscillators leads to lower SNR. Consequently the choice of the oscillator is a tradeoff between high SNR and scanning time. This problem can be avoided by ex-

ploiting a very useful feature of the resonant oscillators. The frequency dependant phase of the oscillator follows the changes in the resonant frequency much faster. Theoretically it takes only one oscillation to detect a frequency change [122]. In practice, however, this is limited to some oscillation cycles which would still be on the micro second scale. Thus the measurement time can be greatly reduced without sacrificing the high Q factor and the high SNR. To maintain the spectral cleanliness of the oscillation it is convenient to drive the oscillator at its resonance frequency independently of damping. In this case an electronic circuit is needed which detects and follows the continuously changing resonant frequency [123]. In practice the appropriate damping and resonance frequency shift are chosen before the experiment. The SPM electronics regulates the damping and the frequency shift by maintaining the tip at the constant hight from the sample.

Possible important parameters of the FM-AFM are [122]:

- Q quality factor of the cantilever ($10^3 - 10^5$),
- $f_0$ free oscillation frequency ($10^{4-6}$ Hz),
- A-amplitude (0.1-1 nm),
- k-spring constant of the cantilever ( 1800 N/m)
- $\Delta f$ frequency shift (2-10 Hz)

The basic idea of the frequency modulated atomic force microscope is the measurement of the resonance frequency of an oscillator. One of the intrinsic properties of a mechanical oscillator is the phase relationship between the exiting force and the oscillation. By applying a mechanical excitation the phase difference is 90° at resonance. The phase difference changes rapidly for frequencies drifting away from the resonance.

One of the most effective methods, to take advantage of this feature, present in today electronic technology is the phase locked loop

(PLL) technique. Its advantages include, for example, capturing of the resonance frequency without its prior knowledge, locking of that frequency (respectively following the frequency changes) and a high spectral cleanness (high SNR).

PLL is basically a closed loop frequency control system, whose functioning is based on the phase sensitive detection of the phase difference between the input and output signals of the controlled oscillator (CO). A PLL consists of three major building blocks: Phase detector, Loop filter, Voltage controlled oscillator (VCO).

A low-pass filter is used to control the dynamic characteristics of the phase-locked loop. If the difference between the input and VCO frequencies is significantly large, the resultant signal is out of the capture range of the loop. Once the loop is phase-locked, the filter only limits the speed of the loop's ability to track changes in the input frequency. In addition, the loop filter provides a sort of short-term memory, ensuring a rapid recapture of the signal if the system is thrown out of lock by a noise transient. However, the design of

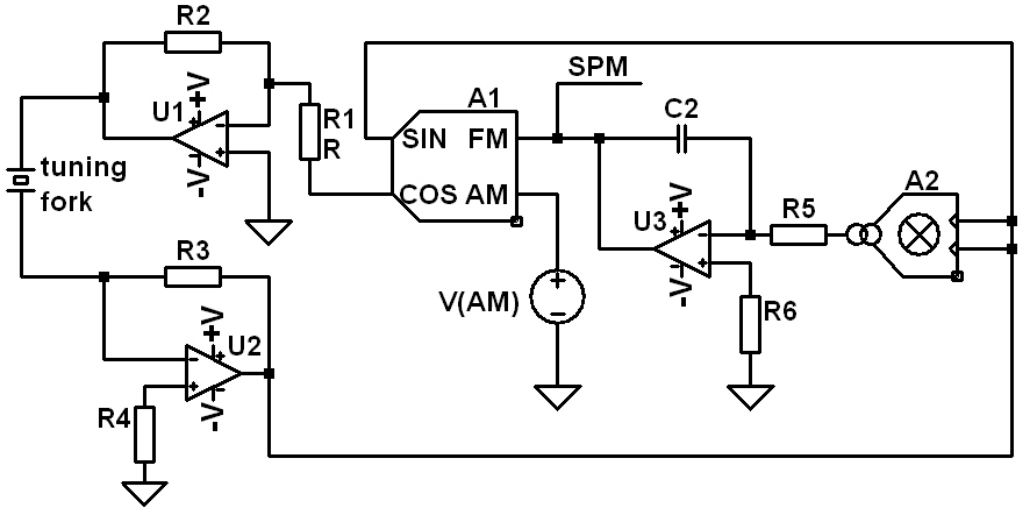


Figure 6.7: Schematic Phase Locked Loop electronic circuit. The tuning fork quartz crystal is kept at its resonance frequency by means of phase comparison between the exciting and transmitted oscillation.

a loop filter represents a compromise in that the parameters of the filter restrict the loop's capture range and speed, such that it would almost be impossible for the phase-locked loop to lock without it.

PLL can be used in combination with an automatic gain (signal level) control system. This would ensure a constant oscillation amplitude of the quartz oscillator even if a damping is applied to it, for example, due to the intended tip contact to the surface or because of changed environment parameters (air pressure, temperature, humidity).

## 6.5 Tip Etching

In spite of some interest in producing silver tips for application in STM in the early days of this technique [124] the development of preparation techniques for silver tips is still challenging. In contrast to the widely used tungsten tips the silver tips do not have oxide layer on their surface due to their chemical stability. This is advantageous for STM applications because no oxide layer handicap the electron transfer between the tip and the sample. This advantage is diminished by the difficulties in etching procedures. Only few etching procedures for silver tips are present in the literature [124, 125, 126]. Unfortunately none of them is satisfying in terms of the tip apex radius, aspect ratio or surface roughness. Well known methods and commercial kits are available for other tip metals (W, Au, Pt-Ir), but not Ag.

In STM applications only the foremost atoms of the tip play a major role for the resolution (tunnelling current) and the conical part of the tip is not of importance. In optical applications, however, the mesoscopic structure of the tip (i.e. radius of curvature at the apex, angle of the cone) plays the central role. Furthermore, the material of the tip has to be chosen according to the spectral region studied due to the relation of the enhancement with its dielectric properties.

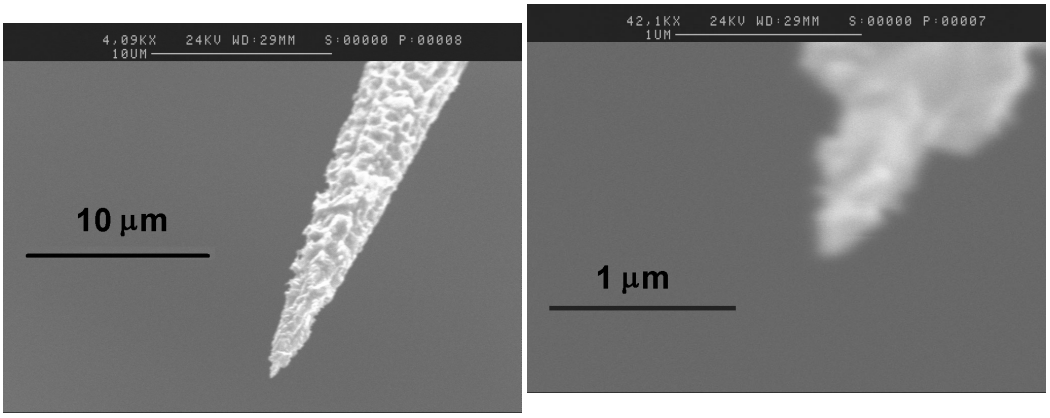


(a) (b)

Figure 6.8: SEM images of a Ag tip etched by the described procedure at different magnifications. The length scale is indicated by bars in the images.

For use in the spectral range from 350 nm to 515 nm, silver has been shown to have a high enhancement factor. Hence, the probes consist of sharp silver tips with an apex radius clearly below 100 nm. To produce silver nano-tips an electrochemical-dynamical etching procedure was developed. It consists of electrochemical etching of a $0.25mm$ diameter silver wire using a highly conductive aqueous solution (a high solubility inorganic $NH_3OH$ salt dissolved in water) and applying a voltage ($1-5V$) between the wire (anode) and a graphite counter electrode (cathode). During the etching the wire is retracted from the solution by a small pitch electric motor. This procedure allows to get sharp tips (apex diameter $< 100nm$) with a shape suitable for A-SNOM applications.

The chemistry of the procedure can be described by the main processes:

$$Ag \rightarrow Ag^+ + e, \tag{6.1}$$

$$NH_4^+ \rightarrow NH_3 + H^+, \tag{6.2}$$

and side reactions

$$Ag^+ + 2NH_3 \rightleftarrows Ag(NH_3)_2^+, \tag{6.3}$$

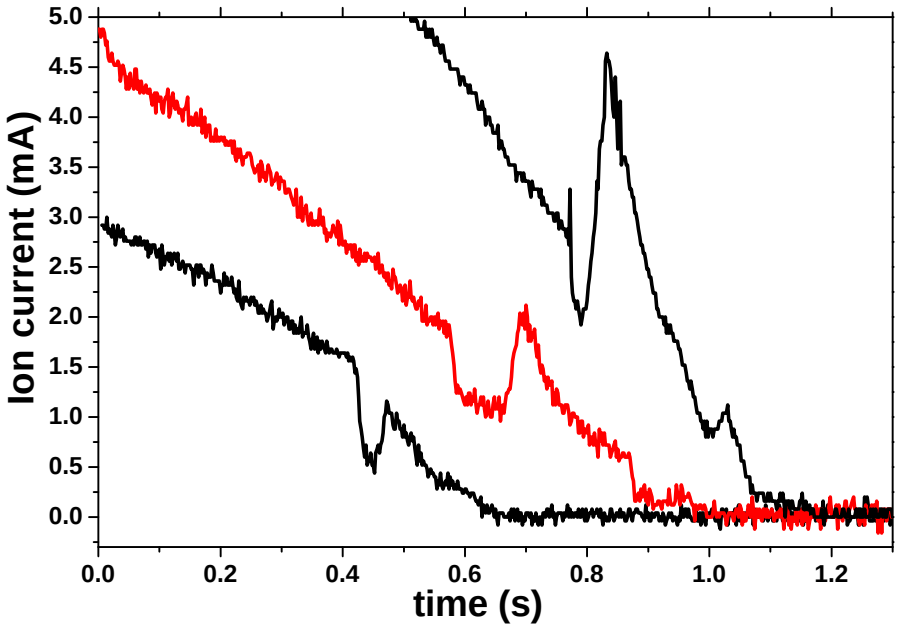


Figure 6.9: Measured tip etching current during the etching procedure. All the curves are measured during the etching in the same solution. From the top to the bottom curve the solution was increasingly degraded due to the consumption of the solvents. To achieve reproducible etching (similar etching rates) in every procedure a regulation of the etching voltage is necessary in order to obtain the same initial current.

$$4Ag^{+} + O_2 \rightarrow 2Ag_2O, \tag{6.4}$$

$$2Ag^{+} + 2OH^{-} - \rightleftarrows Ag_2O + H_2O, \tag{6.5}$$

The products of the side reactions 6.4 and 6.5 are not solvable in the solution and can attach to the tip during the procedure. This can be avoided by slowing down the reaction by reducing the initial current values which gives the side reaction products the time to disperse in the solution instead of building a layer that covers the tip.

Etching of metal tips with apex radii on the nanometer scale requires a fast shutdown of the etching voltage in order to prevent further etching of the tip. From the moment of the separation of the last

wire segment from the tip further etching leads to degradation of the tip apex.

During the finite time of the drop of the meniscus, the transported mass from the tip into the solution is given by the Faraday equation:

$$m = \frac{MQ}{zF}, \tag{6.6}$$

where M is the mol mass, Q is the transferred charge, z the electron charge number of a single ion and F is the Faraday constant. M is known (Ag 107,9 g/mol), Q can be estimated from the tip etching current in Fig.6.9($I \cdot t \approx 4 \times 10^{-4}$ C), z=1 (single electron charge), Faraday constant F: 9.65E4 As/mol.

The estimated mass transfer during the meniscus drop from the tip to the solution is $4 \times 10^{-10}$ kg. This corresponds to $4 \times 10^{4}\ \mu m^3$ of silver (equivalent to a cube of ca 34 $\mu m$). After the disattachment of the last piece of the remaining wire the etching continues for a short time (few ms), but this is sufficient in order to round off the possibly sharp tip.

It is possible to detect the separation of the last segment for example by measuring the etching current. A sudden decrease of the current is expected due to the reduction of the immersed surface area.

A fast voltage switching circuit providing switching times on the nanosecond scale can be realized by a combination of a current-to-voltage converter and a voltage comparator governing a transistor switch. This circuit is shown in Fig.6.10(a) where a video amplifier (LT1193) is used as a current-to-voltage converter. A video amplifier was chosen because of its wide bandwidth of several hundred MHz allowing for fast current detection. The signal from theamplifier LT1193 is conducted to the comparator LT1016 with a switching time of $\approx 7ns$ where it is compared to a fixed voltage representing the tip-solution current reference value. After the voltage from LT1016 falls below the reference value the transistor Q1 is switched by LT1016 trough the impedance matching network. After

(a)

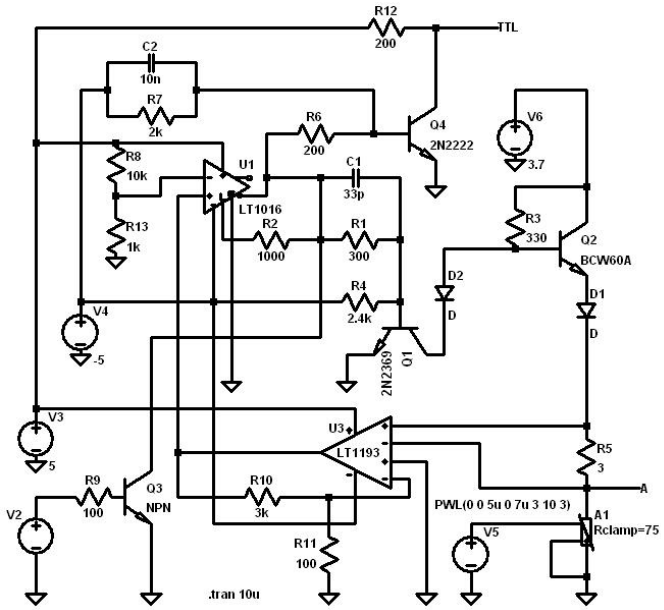


(b)

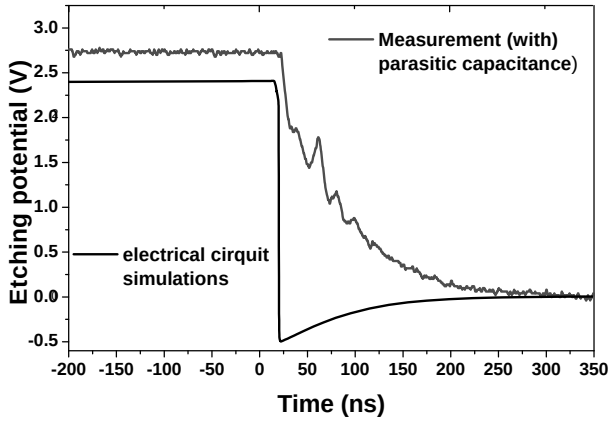


Figure 6.10: (a) Circuit for quick voltage shutdown for Ag tip etching. (b) Simulated (lower line) and measured voltage shutdown transients of the circuit in (a)

that the base of the transistor Q2 is grounded and the current from the fixed voltage source passing the tip-solution junction is stopped. In Fig.6.10(a) a variable resistance A1 (Voltage controlled varactor)is used for simulation of the variable resistance between the tip and the solution. The response time of the circuit in Fig.6.10(a) was simu-

lated using the "SPICE" electrical circuit simulation software and measured during the etching procedure. Transients from simulation and the measurements are shown in Fig.6.10(b). The simulated response time of ca. 20 ns could not be achieved in the experiment probably because of parasitic capacitance in the tip-solution leading to an exponential decrease and oscillations during the voltage drop. Indeed similar behavior was observed in simulations with additional capacities. The reaction time of the circuit is negligible. Thus the achieved switching time could be considered to be near the limit for passive switching for the etching.

New concepts which can be applied to the silver tip etching procedure:

- Limited fixed current instead fixed voltage: this increases the etching time and eventually decreases the roughness due to more uniform etching.
- Annealing of the silver wire for recrystallization and creating larger crystallites increases the chance that the tip apex will be etched from a single monocrystal (works for tungsten wire [127]).

## 6.6 Test measurements

Measurements to test the developed Nano Raman equipment were performed on Rhodamine 6G adsorbed on a silver substrate. To prepare the samples Rhodamine 6G was dissolved in alcohol and applied to the silver substrate. The topography of the prepared samples(Fig. 6.11a) was determined by the STM with the same silver tip which was used for the spectroscopic measurements. Obviously by this method of sample preparation it was not possible to obtain a monolayer of molecules on the surface. Instead Rhodamine 6G agglomerates formed on the surface yielding the distinct features in

the STM image. Although in some cases it was possible to identify agglomerates on the surface, the non-conductivity of the Rhodamine 6G agglomerates turned out to be a severe obstacle for STM measurements.

In order to measure Nano Raman spectra of the adsorbed molecules, the tip and sample were brought into tunnelling contact (upper spectrum Fig. 6.11 b) in a region of the sample with a low density of Rhodamine 6G agglomerates. The sample was excited with the 488 nm line of the $Ar^+$ laser (2.54 eV) at a power of 0.8 mW. To determine the far field background the sample was retracted by about 0.5 $\mu$m from the tip and the lower spectrum was measured (Fig. 6.11b). Both spectra are shown without the luminescence background. Even though the primary aim of the measurement was to test the spectroscopic mode we observed a good agreement with near field Raman spectra reported for Rhodamine 6G [11]. Nevertheless, we do not consider the reported spectrum very reliable, because the sample was retracted from the tip, while the focus of the exciting laser remained on the apex of the tip, so that Rhodamine 6G that might be attached to the tip contributed to the far field background. In order to increase the reliability of the measured near field spectra the tip has to be retracted from the sample and the focus of the exciting laser, and repositioned with a precision in the sub-nanometer range.

Although some practical improvements are necessary, the presented experimental set-up, designed according to the principles introduced above, we are confident to be able to perform reliable spectroscopic measurements with spatial resolution in the nanometer range. Latest results in the literature on tip enhanced Raman spectroscopy are encouraging [128] and confirm the feasibility of the concept.

(a)

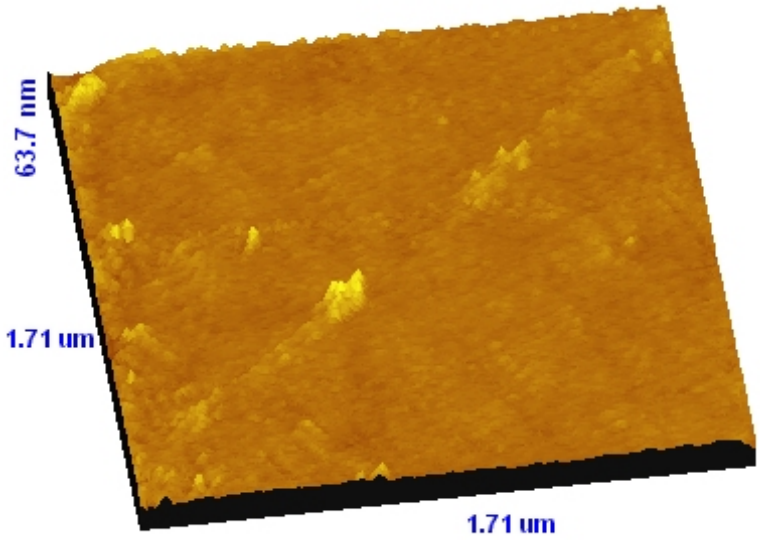


(b)

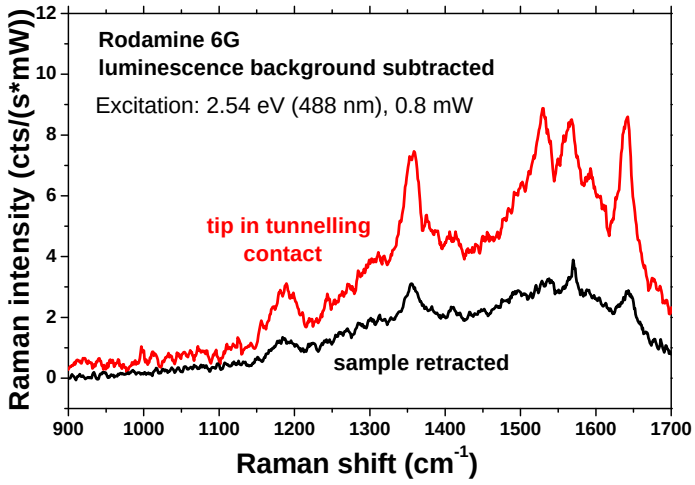


Figure 6.11: Nano Raman test measurements on Rhodamine 6G. On the top: "typical" STM measurements of Rhodamine 6G agglomerates on silver surface. On the bottom: nano Raman measurements with tip in tunnelling (upper spectra), the lower spectrum is taken after retracting the sample by ca. 0.5 $\mu$m.

# Chapter 7

# Summary

In conclusion, micro Raman measurements were performed on low dimensional semiconductor structures. Averaging on nano structure ensembles (usually on as grown samples) were avoided by measuring on single structures. For this purpose low density as grown samples and selected single structures were used. For the first time surface vibrations on single GaAs nanowires were measured by this approach. A possible shape effect on Raman spectra of ZnO nano wires was identified. Thermal effects which have important implications on Raman spectra were investigated. The anharmonic effect screens the properties of nano structures distorting the phonon line shapes. Reducing substantially the excitation laser power it was possible to obtain unperturbed Raman spectra of nano structures. It is also possible to extract information on non-perturbed phonon structure by investigating the dependency of spectra on laser heating. The anharmonic broadening and energy shifts were successfully described within the phenomenological anharmonic oscillator model. Successful fits of Raman spectra from single Si nano-wires at different excitation powers (temperatures) verify the validity of the anharmonic oscillator model. Due to comparably large sizes of the nanostructures (in the range of 100 nm) no volume confinement effects were expected nor observed. Surface and folding effects play a major role for nano structures of this size. Potential Si nanotube

spectra were measured by micro-Raman set-up and compared with a DFT ab-initio calculation. The agreement between the measurement and the calculation is not yet satisfying. Thus new measurements will be performed in order to confirm the presence of Si-H bonds in the structure and new calculations considering modified hydrogen bonds are on the way.

Even though micro Raman spectroscopy reveals the internal structure of the crystals, it gives only average information from the spatially resolved area (1 $\mu m^2$). The attribution of the revealed properties to specific nano structure or locations within the nano structures seems impossible without an significant improvement of spatial resolution.

For this purpose an apertureless scanning near field optical microscope (a-SNOM) set-up was developed. Scanning Probe Microscopy (SPM) equipment was integrated into confocal Raman spectroscopy apparatus. Special attention was focused on the possibility to use a wide spread of excitation energies in the same set-up, from near UV (350nm) to red (633 nm). That implies that several radiation sources were integrated into the set-up which renders the construction of such integrated apparatus complicated. First of all because of its extensive dimensions and vibrational isolation.

SPM technique require the utilization of sharp tips in nanometric proximity to the sample. In a-SNOM the optical field is amplified by the tip according to its shape and material properties. In order to exploit the UV spectral range, the use of silver tips was identified as one of the options. Because of lack of appropriate preparation methods in literature a new preparation technique for silver tips was developed. Though the procedure is not yet optimized first test measurements utilizing these tips were performed on Rhodamine 6G on top of a silver substrate. First results prove the functionality of the set-up. It is expected that further improvement of the silver tip properties will enable for nanometric resolution spectroscopy.

# Bibliography


[1] M. A. Herman, W. Richter, and H. Sitter. *Epitaxy: Physical Principles and Technical Implementation*. SpringerVerlag, New York, 2004.

[2] C.B. Murray, D.J. Norris, and M.G. Bawendi. Synthesis and characterization of nearly monodisperse CdE (E = S, Se, Te) semiconductor nanocrystallites. *J. Am. Chem. Soc.*, **115**:8706, 1993.

[3] G. Binnig, H. Rohrer, C. Gerber, and E. Weibel. Tunneling through a controllable vacuum gap. *Appl. Phys. Lett.*, **40**:178–180, 1982.

[4] D.W. Pohl, W. Denk, and M. Lanz. Optical stethoscopy: Image recording with resolution lambda/20. *Appl. Phys. Lett.*, **44**:651, 1984.

[5] B. Hecht, B. Sick, and U.P. Wild et al. Scanning near-field optical microcopy with aperture probes: Fundamentals and applications. *J. Chem. Phys.*, **112**:7761–7774, 2000.

[6] L. Novotny and C. Hafner. Light propagation in a cylindrical waveguide with a complex, metallic, dielectric function. *Phys. Rev. E*, **50**:4094, 1994.

[7] M. Goetz, D. Drews, D.R.T. Zahn, and R. Wannemacher. Near-field Raman spectroscopy of semiconductor heterostructures and CVD-diamond layers. *J. of Luminescence*, **76**:306, 1998.

[8] C.L. Jahncke, M.A. Paesler, and H.D. Hallen. Raman imaging with near-field scanning optical microscopy. *Appl. Phys. Lett.*, **67**:2483, 1995.

[9] F. Zenhausern, M.P.O'Boyle, and H.K. Wickramasinghe. Apertureless near-field optical microscope. *Appl. Phys. Lett.*, **65**:1623, 1994.

[10] G. Binnig, C.F. Quate, and C. Gerber. Atomic force microscope. *Phys. Rev. Lett.*, **56**:930–933, 1986.

[11] N. Hayazawa, Y. Inouye, Z. Sekkat, and S. Kawata. Near-field Raman scattering enhanced by a metallized tip. *Chem. Phys. Lett.*, **335**:369, 2001.

[12] Mark S. Anderson. Locally enhanced raman spectroscopy with an atomic force microscope. *Appl. Phys. Lett.*, **76**:3130, 2000.

[13] B. Pettinger, B. Ren, G. Picardi, R. Schuster, and G. Ertl. Nanoscale Probing of Adsorbed Species by Tip-Enhanced Raman Spectroscopy. *Phys. Rev. Lett.*, **92**:096101, 2004.

[14] M.A. Reed, J.N. Randall, R.J. Aggarwal, R.J. Matyi, T.M. Moore, and A.E. Wetsel. Observation of discrete electronic states in a zero-dimensional semiconductor nanostructure. *Phys. Rev. Lett.*, **60**:535, 1988.

[15] G. D. Sanders and Yia-Chung Chang. Optical properties of free-standing silicon quantum wires. *Appl. Phys. Lett.*, **60**:2525, 1992.

[16] J. von Behren, T. van Buuren, M. Zacharias, E. H. Chimowitz, and P. M. Fauchet. Quantum confinement in nanoscale Si: the correlation of size with band gap and luminescence. *Solid State Communication*, **105**:317, 1998.

[17] J. Motohisa, J. Noborisaka, J. Takeda, M. Inari, and T. Fukui. Catalyst-free selective-area movpe of semiconductor nanowires on (111)b oriented substrates. *J. of Crys. Growth*, **272**:180, 2004.

[18] R. S. Wagner and W. C. Ellis. Vapor-liquid-solid mechanism of single crystal growth. *Appl. Phys. Lett.*, **4**:89, 1964.

[19] Yi Cui, Lincoln J. Lauhon, Mark S. Gudiksen, Jianfang Wang, and Charles M. Lieber. Diameter-controlled synthesis of single-crystal silicon nanowires. *Appl. Phys. Lett.*, **78**:2214, 2001.

[20] P. Paiano, P. Prete, N. Lovergine, and A. M. Mancini. Size and shape control of gaas nanowires grown by metalorganic vapor phase epitaxy using tertiarybutylarsine. *J. Appl. Phys.*, **100**:094305, 2006.

[21] P. Paiano, P. Prete, E. Speiser, N. Lovergine, W. Richter, L. Tapfer, and A.M. Mancini. GaAs nanowires grown by Au-catalyst-assisted MOVPE using tertiarybutylarsine as group-V precursor. *J. of Crys. Growth*, **298**:620, 2007.

[22] M. Fernández-Garcý, A. Martýnez-Arias, J. C. Hanson, and J. A. Rodriguez. Nanostructured Oxides in Chemistry: Characterization and Properties. *Chem. Rev.*, **104**:4063, 2004.

[23] Varghese Swamy and Barry C. Muddle. Size-dependent modifications of the Raman spectrum of rutile $TiO_2$. *Appl. Phys. Lett.*, **89**:163118, 2006.

[24] A. Diéguez, A. Romano-Rodrýguez, A. Vila, and J. R. Morante. The complete Raman spectrum of nanometric SnO2 particles. *J. Appl. Phys.*, **90**3:1550, 2001.

[25] T. Ruf. *PhononRaman Scattering in Semiconductors, Quantum Wells and Superlattices, Springer Tracts in Modern Physics*. Sringer-Verlag, Berlin, Heidelberg, 1998.

[26] Pasquale Pavone. Old and new aspects in lattice-dynamical theory. *J. Phys.: Condens. Matter*, **13**:7593, 2001.

[27] Paolo Giannozzi, Stefano de Gironcoli, Pasquale Pavone, and Stefano Baroni. Ab initio calculation of phonon dispersions in semiconductors. *Phys. Rev. B*, **43**:7231, 1991.

[28] Frank H. Stillinger and Thomas A. Weber. Computer simulation of local order in condensed phases of silicon. *Phys. Rev. B*, **31**:5262, 1985.

[29] T. Thonhauser and G. D. Mahan. Phonon modes in Si [111] nanowires. *Phys. Rev. B*, **69**:075213, 2004.

[30] A. Milekhin, D. A. Tenne, and D. R. T. Zahn. *Quantum Dot Structures: Raman and Infrared Spectroscopy in Quantum Dots and Nanowires, edited by Supriyo Bandyopadhyay and Hari Singh Nalwa*. American Scientific Publishers, 2003.

[31] H. Richter, Z.P. Wang, and L. Ley. The one phonon Raman Spectrum in microcystalline Silicon. *Solid State Communications*, **39**:625, 1981.

[32] I.H. Campbell and P.M. Fauchet. The effect of microcrystal size and shape on the phonon Raman spectra of cyrystalline Semiconductors. *Solid State Communications*, **58**:739, 1986.

[33] Ranber Singh and S. Prakash. Phenomenological description of phonon confinement in semiconductor nanocrystals. *Surface Science*, **532**:780, 2003.

[34] S. Piscanec, A.C. Ferrari, M. Cantoro, S. Hofmann, J.A. Zapien, Y. Lifshitz, S.T. Lee, and J. Robertson. Raman Spectrum of silicon nanowires. *Materials Science and Engineering*, **C 23**:931, 2003.

[35] Somnath Bhattacharyya and Saumyadip Samui. Phonon confinement in oxide-coated silicon nanowires. *Appl. Phys. Lett.*, **84**:1564, 2004.

[36] Y.M. Yang, X.L. Wu, G.S. Huang, D.S. Hu, and G.G. Siu. *Physics Letters*, **A 338**:379, 2005.

[37] R. Wang. Raman spectral study of silicon nanowires: High-order scattering and phonon confinement effects. *Phys. Rev. B*, **61**:16827, 2000.

[38] C. Trallero-Giner, F. García-Moliner, V. R. Velasco, and M. Cardona. Analysis of the phenomenological models for long-wavelength polar optical modes in semiconductor layered systems. *Phys. Rev. B*, **45**:11944, 1992.

[39] E. Roca, C. Trallero-Giner, and M. Cardona. Polar optical vibrational modes in quantum dots. *Phys. Rev. B*, **49**:13704, 1994.

[40] Xinhua Hu and Jian Zi. Reconstruction of phonon dispersion in Si nanocrystals. *J. Phys.: Condens. Matter*, **14**:L671, 2002.

[41] C.Colvard, T.A.Gant, M.V. Klein, R. Merlin, R. Fisherand H. Morcoc, and A.C. Gossard. Folded acoustic and quantized optic phonons in (GaAl)As superlattices. *Phys. Rev. B*, **31**:2080, 1985.

[42] Vladimir A. Fonoberov and Alexander A. Balandin. Interface and confined polar optical phonons in spherical ZnO quantum dots with wurtzite crystal structure. *phys. stat. sol. (c)*, **1**:2650, 2004.

[43] Aian Zi, H. Büscher, C. Falter, W. Ludwig, Kaiming Zhang, and Xide Xie. Raman shifts in Si nanocrystals. *Appl. Phys. Lett.*, **69**:200, 1996.

[44] S. Guha, J. Menendez, J. B. Page, and G. B. Adams. Temperature dependence of the first-order Raman scattering by phonons in Si, Ge, and $\beta$-Sn: Anharmonic effects. *Phys. Rev. B*, **53**:13106, 1996.

[45] Wei Cheng and Shang-Fen Ren. Calculations on the size effects of Raman intensities of silicon quantum dots. *Phys. Rev. B*, **65**:205305, 2002.

[46] C. Falter. A unifying approach to lattice dynamical and electronic properties of solids. *Physics Reports*, **164**:1, 1988.

[47] Sammy Go, Heinz Bilz, and Manuel Cardona. Bond Charge, Bond Polarizability, and Phonon Spectra in Semiconductors. *Phys. Rev. Lett.*, **34**:580, 1975.

[48] S. Baroni, P. Giannozzi, and E. Molinari. Phonon spectra of ultrathin GaAs/AlAs superlattices: An ab initio calculation. *Phys. Rev. B*, **41**:3870, 1990.

[49] E. Molinari, S. Baroni, P. Giannozzi, and S. De Gironcoli. Effects of disorder on the Raman spectra of GaAs/AlAs superlattices. *Phys. Rev. B*, **45**:4280, 1992.

[50] J. Menendez and M. Cardona. Temperature dependence of the first-order Raman scattering by phonons in Si, Ge and $\alpha$-Sn: Anharmonic effects. *Phys. Rev. B*, **29**:2051, 1984.

[51] M. Balkanski, R. Wallis, and E. Haro. Anharmonic effects in light scattering due to optical phonons in silicon. *Phys. Rev. B*, **28**:1928, 1983.

[52] H. Tang and I. Herman. Raman microprobe scattering of solid silicon and germanium at the melting temperature. *Phys. Rev. B*, **43**:2299, 1991.

[53] A. Deberanrdi, S. Baroni, and E. Molinari. Anharmonic Phonon Lifetimes in Semiconductors from Density-Functional Perturbation Theorie. *Phys. Rev. Lett.*, **75**:1819, 1995.

[54] U. Fano. Effects of configuration interaction on intensities and phase shifts. *Phys. Rev.*, **124**:1866, 1961.

[55] Hua Tung and Irving P. Herman. Raman microprobe scattering of solid silicon and germanium at the melting temperature. *Phys. Rev. B*, **43**:2299, 1991.

[56] K.W. Adu, Q. Xiong, H.R. Gutierrez, G. Chen, and P.C. Eklund. Raman scattering as a probe of phonon confinement and surface optical modes in semiconducting nanowires. *Applied Physics A*, **85**:287, 2006.

[57] Jayhoon Chung, Ji-Ping Zhou, and Lew Rabenberg. Mean inner potentials in oxidized germanium nanowires by electron holography. *Microsc Microanal.*, **11**(Suppl 2):588, 2005.

[58] R. Enderlein. Optical-phonon modes of circular quantum wires. *Phys. Rev. B*, **47**:2162, 1993.

[59] J. L. Vega R. Guantes and S. Miret-Arte´s. Hamiltonian theory for vibrational line shapes of atoms adsorbed on surfaces. *JOURNAL OF CHEMICAL PHYSICS*, **120**:10768, 2004.

[60] M. Minsky. Memoir on inventing the confocal scanning microscope. *Scanning*, **10**:128, 1961.

[61] G.S. Duesberg, W.J. Blau, H.J. Byrne, J. Muster, M. Burghard, and S. Roth. Experimental observation of individual single-wall nanotube species by raman microscopy. *Chem. Phys. Lett.*, **310**:8, 1999.

[62] G. S. Duesberg, I. Loa, M. Burghard, K. Syassen, and S. Roth. Polarized Raman Spectroscopy on Isolated Single-Wall Carbon Nanotubes. *Phys. Rev. Lett.*, **85**:5436, 2000.

[63] A. Jorio, A. G. Souza Filho, G. Dresselhaus, M. S. Dresselhaus, A. K. Swan, M. S. Ünlü, B. B. Goldberg, M. A. Pimenta, J. H. Hafner, C. M. Lieber, and R. Saito. G-band resonant Raman study of 62 isolated single-wall carbon nanotubes. *Phys. Rev. B*, **65**:155412, 2002.

[64] A. Jorio, M.A. Pimenta1, A.G. Souza Filho, R. Saito, G. Dresselhaus, and M.S. Dresselhaus. Characterizing carbon nanotube samples with resonance Raman scattering. *New J. of Phys.*, **5**:139.1, 2003.

[65] J. Maultzsch, S. Reich, and C. Thomsen. Raman scattering in carbon nanotubes revisited. *Phys. Rev. B*, **65**:233402–1, 2002.

[66] R. Loudon. Theory of the first-order raman effect in crystals. *Proc. Royal Soc.*, **A275**:218, 1963.

[67] W. Hayes and R. Loudon. *Light Scattering in Solids*. J. Wiley and Sons, New York, 1978.

[68] W. Richter. *Springer Tracts in Modern Physics* **Vol. 78**, *Resonant Raman Scattering in Semiconductors, ed. by G. Höhler*. Springer, Berlin, Heidelberg, New York, 1976.

[69] M. Cardona. *Topics in Applied Physics* **Vol. 50**, *Light Scattering in Solids II, ed. by M. Cardona and G. Güntherodt*. Springer, Berlin, Heidelberg, New York, 1982.

[70] M. Cardona. *Light Scattering in Solids V. Superlattices and Other Microstructures, ed. by M. Cardona and G. Güntherodt*. Springer-Verlag Berlin and Heidelberg GmbH & Co. K, 1989.

[71] N. Esser and J. Geurts. *Optical Characterization of Epitaxial Semiconductor Layers, Ed.: G. Bauer, W. Richter*. Springer, Berlin, Heidelberg, New York, 1996.

[72] A. Pinczuk and E. Burstein. *Topics in Applied Physics* **Vol. 8**, *Light Scattering in Solids, ed. by M. Cardona and G. Güntherodt*. Springer, Berlin, Heidelberg, New York, 1975.

[73] J. F. Geisz, D. J. Friedman, J. M. Olson, S. R. Kurÿtz, and B. M. Keyes. Photocurrent of 1 eV GaInNAs lattice-matched to GaAs. *J. Cryst. Growth*, **195**:401, 1998.

[74] M. Kondow, S. Nakatsuka, T. Kitatani, Y. Yazawa, and M. Okai. Room-Temperature Pulsed Operation of GaInNAs Laser Diodes with Excellent High-Temperature Performance. *Jpn. J. Appl. Phys.*, **35**:5711, 1996.

[75] J. S. Wang, A. R. Kovsh, L. Wei, J. Y. Chi, Y. T. Wu, P. Y. Wang, and V. M. Ustinov. MBE growth of high-quality GaAsN bulk layers. *Nanotechnology*, **12**:430, 2001.

[76] Markus Weyers and Michio Sato. Growth of GaAsN alloys by low-pressure metalorganic chemical vapor deposition using plasma-cracked $NH_3$. *Appl. Phys. Lett.*, **62**:1396, 1993.

[77] H. Ch. Alt, A. Yu. Egorov, H. Riechert, B. Wiedemann, J. D. Meyer, R. W. Michelmann, and K. Bethge. Infrared absorption study of nitrogen in N-implanted GaAs and epitaxially grown $GaAs_{1-x}N_x$ layers. *Appl. Phys. Lett.*, **77**:3331, 2000.

[78] A. M. Mintairov, P. A. Balagnov, V. G. Melehin, N. N. Faleev, J. L. Merz, Y. Qiu, S. A. Nikishin, and H. Temkin. Ordering effects in Raman spectra of coherently strained GaAs1-xNx. *Phys. Rev. B*, **56**:15863, 1997.

[79] T. Prokofyeva, T. Sauncy, M. Seon, M. Holtz, Y. Qui, S. Nikishin, and H. Temkin. Raman studies of nitrogen incorporation in $GaAs_{1-x}N_x$. *Appl. Phys. Lett.*, **73**:1409, 1998.

[80] B. H. Armstrong. Spectrum line profiles: The Voigt function. *J. Quant. Spectrosc. Radiat. Transfer*, **7**:61, 1967.

[81] Marian A. Herman, Wolfgang Richter, and Helmut Sitter. *Epitaxy, Physical Principles and Technical Implementation*. Springer-Verlag Berlin Heidelberg New York, 2004.

[82] J. Serrano, F. Widulle, A. H. Romero, A. Rubio, R. Lauck, and M. Cardona. Dependence of phonon widths on pressure and isotopic mass: Zno. *phys. stat. sol. (b)*, **235**:260, 2003.

[83] A. C. Ferrari, S. Piscanec, S. Hoffmann, M. Cantoro, C. Ducati, and J. Robertson. Raman Spectroscopy of Silicon Nanowires: Phonon Confinement and Anharmonic Phonon Processes. *AIP Conf. Proc.*, **685**:507, 2003.

[84] R. J. Nemanich, D. K. Biegelsen, R. A. Street, and L. E. Fennell. Raman scattering from solid silicon at the melting temperature. *Phys. Rev. B*, **29**:6005, 1984.

[85] E. Speiser, T. Schmidtling, K. Fleischer, N. Esser, and W. Richter. In-situ Raman Spectroscopy on III-V semiconductors at high temperature in MOVPE. *phys. stat. sol (c)*, **0**:2949–2955, 2003.

[86] Rajeev Gupta, Q. Xiong, G. D. Mahan, and P. C. Eklund. Surface optical phonons in gallium phosphide nanowires. *Nano Letters*, **3**:1745, 2003.

[87] Bo E. Sernelius. *Surface Modes in Physics*. Wiley-VCH, New York, 2001.

[88] J. F. Scott. Uv Resonant Raman Scattering in ZnO. *Phys. Rev. B*, **2**:1209, 1970.

[89] R. H. Callender, S. S. Sussman, M. Selders, and R. K. Chang. Dispersion of Raman Cross Section in CdS and ZnO over a Wide Energy Range. *Phys. Rev. B*, **7**:3788, 1973.

[90] J. M. Calleja and M. Cardona. Resonant Raman scattering in ZnO. *Phys. Rev. B*, **16**:3753, 1977.

[91] C. A. Arguello, D. L. Rousseau, and S. P. S. Porto. First-order raman effect in wurtzite-type crystals. *Phys. Rev.*, **181**:1351, 1969.

[92] M. Rajalakshmi, A.K. Arora, B.S. Bendre, and S. Mahamuni. Optical phonon confinement in zinc oxide nanoparticles. *J. Appl. Phys.*, **87**:5, 2000.

[93] O.K. Kim and W.G. Spitzer. Infrared reflectivity and Raman spectra Of $Ga_{1-x}Al_xAs$ mixed crystals. *J. Appl. Phys.*, **50**(6):4362, 1979.

[94] I. F. Chang and S. S. Mitra. Optical Phonons in $Ga_{1-x}Al_xAs$ Mixed Crystals: A Modified Random-Element Isodisplacement-Model Calculation. *Phys. Rev. B*, **2**:1215, 1970.

[95] G. Seifert, Th. Koehler, H. M. Urbassek, E. Hernandez, and Th. Frauenheim. Tubular structures of silicon. *Phys. Rev. B*, **63**:193409, 2001.

[96] R.Q. Zhang, S.T. Lee, Chi-Kin Law, Wai-Kee Li, and Boon K. Teo. Silicon nanotubes: Why not? *Chemical Physics Letters*, **364**:251, 2002.

[97] S.Y. Jeong, J.Y. Kim, H.D. Yang, B.N. Yoon, S.-H. Choi, H.K. Kang, and Y.H. Lee C.W. Yang. Synthesis of silicon nanotubes on porous alumina using molecular beam epitaxy. *Advanced Materials*, **15**:1172, 2003.

[98] M. De Crescenzi, P. Castrucci, M. Scarselli, M. Diociaiuti, Prajakta S. Chaudhari, C. Balasubramanian, Tejashree M. Bhave, and S. V. Bhoraskar. Experimental imaging of silicon nanotubes. *Appl. Phys. Lett.*, **86**:231901, 2005.

[99] Deborah Prezzi. PhD Fellow, Università di Modena e Reggio Emilia, private communication.

[100] H. Bethe. Theory of diffraction by small holes. *Phys. Rev.*, **66**:163, 1944.

[101] C.J. Bouwkamp. Diffraction theory. *Rep. Prog. Phys.*, **17**:35, 1954.

[102] L. Novotny and B. Hecht. *Principles of Nano-Optics*. Cambridge University Press, 2006.

[103] Yves C. Martin, Hendrik F. Hamann, and H. Kumar Wickramasinghe. Strength of the electric field in apertureless near-field optical microscopy. *J. Appl. Phys.*, **89**:5774, 2001.

[104] A. L. Demming F. Festy and D. Richards. Plasmon resonances on metal tips: Understanding tip-enhanced Raman scattering. *Tne Journal of Chemical Physics*, **122**:184716, 2005.

[105] A.V. Goncharenko, Hung-Chih Chang, and Juen-Kai Wang. Electric near-field enhancing properties of a finite-size metal conical nano-tip. *Ultramicroscopy*, **107**:151, 2007.

[106] Pavel I. Geshev, Stefan Klein, Tobias Witting, Klaus Dickmann, and Michael Hietschold. Calculation of the electric-field enhancement at nanoparticles of arbitrary shape in close proximity to a metallic surface. *Phys. Rev. B*, **70**:075402, 2004.

[107] Ryan M. Roth, Nicolae C. Panoiu, Matthew M. Adams, Richard M. Osgood Jr., Catalin C. Neacsu, and Markus B. Raschke. Resonant-plasmon field enhancement from asymmetrically illuminated conical metallic-probe tips. *OPTICS EXPRESS*, **14**(7):2921, 2006.

[108] Lukas Novotny, Erik J. Sanchez, and X. Sunney Xie. Near-Field optical imaging using metal tips illuminated by higher-order Hermite Gaussian beams. *Ultramicroscopy*, **71**:21Ð29, 1998.

[109] R. Dorn, S. Quabis, and G. Leuchs. Sharper focus for a radially polarized light beam. *Phys. Rev. Lett.*, **91**:233901, 2003.

[110] C.L. Jahncke, H.D. Hallen, and M.A. Paesler. Nano-Raman Spectroscopy and Imaging with a Near-Field Scanning Optical Microscope. *J. of Raman Spec.*, **27**:579, 1996.

[111] M. Fleischmann, P.J. Hendra, and A.J. McQuillan. Raman spectra of pyridine adsorbed at a silver electrode. *Chem. Phys. Lett.*, **26**:163, 1974.

[112] M. Moskovits. Surface-enhanced spectroscopy. *Rev. Mod. Phys.*, **57**:783, 1985.

[113] T. Ichimura, N. Hayazawa, M. Hashimoto, Y. Inouye, and S. Kawata. Tip-Enhanced Coherent Anti-Stokes Raman Scattering for Vibrational Nanoimaging. *Phys. Rev. Lett.*, **92**:220801, 2004.

[114] Cecilia Noguez. Optical properties of isolated and supported metal nanoparticles. *Chem. Phys. Lett.*, **27**:1204, 2005.

[115] A. Hartschuh, E.J. Sánchez, X.S. Xie, and L Novotny. High-Resolution Near-Field Raman Microscopy of Single-Walled Carbon Nanotubes. *Phys. Rev. Lett.*, **90**:095503, 2003.

[116] N. Hayazawa, T. Yano, H. Watanabe, Y. Inouye, and S. Kawata. Detection of an individual single-wall carbon nanotube by tip-enhanced near-field raman spectroscopy. *Chem. Phys. Lett.*, **376**:174, 2003.

[117] Y. Saito, M. Motohashi, and N. Hayazawa. Nanoscale characterization of strained silicon by tip-enhanced Raman spectroscope in reflection mode. *Appl. Phys. Lett.*, **88**:143109, 2006.

[118] L Novotny, R.X. Bian, and X.S. Xie. Theory of nanometric optical tweezers. *Phys. Rev. Lett.*, **79**:645, 1997.

[119] P.I. Geshev, F. Demming, J. Jersch, and K. Dickmann. Calculation of the temperature distribution on laser-illuminated scanning probe tips. *Appl. Phys. B*, **70**:91, 2000.

[120] Khaled Karrai and Robert D. Grober. Piezoelectric tip-sample distance control for near field optical microscopes. *Appl. Phys. Lett.*, **66**:1842, 1995.

[121] T. R. Albrecht, P. Grütter, D. Horne, and D. Rugar. Frequency modulation detection using high-Q cantilevers for enhanced force microscope sensitivity. *J. Appl. Phys.*, **69**:668, 1991.

[122] Franz J. Giessibl. Advances in atomic force microscopy. *Reviews of Modern Physics*, **75**:949, 2003.

[123] Byung I. Kim. Direct comparison between phase locked oscillator and direct resonance oscillator in the noncontact atomic force microscopy under ultrahigh vacuum. *Reviews of Scientific Instruments*, **75**:5035, 2004.

[124] A. A. Gorbunov, B. Wolf, and J. Edelmann. The use of silver tips in scanning tunneling microscopy. *Rev. Sci. Ins.*, **64**:2393, 1993.

[125] K. Dickmann, F. Demming, and J. Jersch. New etching procedure for silver scanning tunneling tips. *Rev. Sci. Ins.*, **67**:845, 1996.

[126] M. Iwami, Y. Uehara, and S. Ushioda. Preparation of silver tips for scanning tunneling microscopy imaging. *Rev. Sci. Ins.*, **69**:4010, 1998.

[127] M. Greiner and P. Kruse. Recrystallization of tungsten wire for fabrication of sharp and stable nanoprobe and field-emitter tips. *Rev. Sci. Ins.*, **78**:026104, 2007.

[128] Neil Anderson, Achim Hartschuh, and Lukas Novotny. Chirality Changes in Carbon Nanotubes Studied with Near-Field Raman Spectroscopy. *Nano Letters*, **7**(3):577, 2007.

# Ringraziamenti

Un sentito ringraziamento va al dipartimento di Fisica dell'Università di Roma Tor Vergata, per avermi dato la possibilità di svolgere, grazie alla borsa di studio assegnatami, il mio dottorato in Fisica. In particolare, all'interno del dipartimento, ringrazio vivamente il coordinatore del corso di dottorato Prof. Giorgio Picozza e la segretaria del dottorato Anna Minella per il loro tempo dedicato ai miei tre anni qui trascorsi, Il direttore del dipartimento di fisica dell'Università di Roma Tor Vergata Prof. Rodolfo Del Sole, del quale ho potuto apprezzare l'ottima capacità amministrativa mostrata in questi tre anni di mia permanenza presso lo stesso dipartimento e allo stesso tempo quella del suo vice direttore Prof. Maurizio De Crescenzi.

Ringrazio il Prof. Wolfgang Richter con il quale ho condiviso il trasferimento dall'Università tecnica di Berlino a quella di Roma e che mi ha dato la possibilità di portare avanti il mio progetto. Un vivo ringraziamento và anche ai professori e ricercatori che hanno dedicato il loro tempo per i seminari relativi ai corsi di dottorato, i quali ho reputato molto formativi dal punto di vista della cultura generale nella fisica.

È doveroso ringraziare l'officina meccanica dell´Università di Tor Vergata, in particolare agli specialisti dediti ai lavori per il dipartimento di Fisica i quali si sono prodigati per la realizzazione delle innumerevoli parti meccaniche da noi commissionategli e che hanno realizzate con estrema precisione e migliorati grazie ai loro suggerimenti e esperienza.

Uno speciale ringraziamento va in fine all'Università di Roma Tor vergata e al suo Magnifico Rettore per aver elargito a favore del nostro gruppo di ricerca, gli ingenti fondi per la "grande attrezzatura" che hanno permesso di sviluppare l'intero setup sperimentale sul quale si è articolato il mio lavoro di tesi di dottorato, inoltre, tale setup è attualmente il cardine del nostro lavoro di ricerca e le sue potenzialità saranno sfruttate nei nostri progetti di ricerca e in eventuali collaborazioni.